Chapter 1

1.1. Introduction

In recent years, the semiconductors nanostructures have became the essential study in research areas especially among the various fields of nanoscience and technology [1-5]. The novel properties i.e. structural, optical and electrical properties of semiconductors nanocrystals mainly depend on the different aspects such as crystal size, shape as well as crystalline nature. Therefore, the particle size, shape and crystal structures of the semiconductors nanoparticles are the fundamental features to control the nanocrystals properties. Different types of semiconductor nanocrystals and metal chalcogenides nanocrystals are too much significant due to their novel physical, chemical, luminescence properties and vast potential applications in research field [6-9]. Structural, optical as well as electrical properties of the semiconducting nanostructures are altered from their bulk properties which are due to the variation of quantum confinement of the electron and surface to volume ratio [10-12]. Semiconducting nanoparticles are of great interest due to their different types of applications in different field of areas such as solar cell [13-14], gas sensor [15-16], biosensor [17], Li-ion battery [18-19], photodector [20-21], light emitting diodes (LED) [22], electrochemical capacitors [23] etc.

The environmental pollution is a dangerous problem in our universe. Harmful gases are mainly responsible for the cause of pollution. Therefore, it is very important to become aware of the explosive, highly flammable and toxic gases. There are different types of toxic as well as dangerous gases which may effect on human beings. It is simply fact that the gas sensing characteristics of metal sulfide semiconducting nanomaterial is related to the electron transfer mechanism from the surface of the materials when the respective gases are flowed to the materials. Therefore, the size of crystal, morphology, percentage of elements, surface

activities etc. are the crucial parameters for the activity of gas sensing performances [24-26]. Due to their excellent sensitivity, fast response and fast recovery time, moderate stability and selectivity, metal sulfide nanoparticles used for gas sensor [27-30]. Recently, the demand for energy in the world is increasing rapidly. However, the supply of nonrenewable energy is not sufficient to make up with the rising demand of energy in a tenable way. Peoples are searching highly efficient and renewable energy sources to maintain communal and financial development in the world. Different types of renewable energy sources from the natural world for instance water power, wind power, biofuel, tide, sunshine flux, terrestrial heat etc. have been used to make our world for constantly work [31-33]. But, due to some limitations, these renewable energies such as water power, wind power, biofuel, tide and terrestrial heat are unable to reach to all the peoples in the world. For this purpose, the energy coming from sun is the most valuable and ideal energy source. Hence, solar energy can be considered as the alternate solution for clean, abundant, and renewable energy sources. The current approach is to construct economical photovoltaic devices and to enhance its efficiency [34-37]. Tin sulfide (SnS) is a new class of semiconducting material (group IV-VI) which can be applied in photovoltaic and optoelectronic devices [38-41]. It has direct band gap energy of 1.3 eV, moderate bohr radius of ~ 9.5 nm [42], low cost, greater absorption coefficient ($>10^4$ cm^{-1}) in the optical region as well as it can shows remarkable optical and electrical properties [43-46]. It is mainly belongs in the phase of orthorhombic crystal structure where lattice parameters are $a = 0.432, b = 1.121$ and $c = 0.399$ nm. SnS has double layer structure where Sn and S are bounded by van der waals force [47]. The elements of SnS nanoparticles are not posing on human beings and environmental hazards [48]. SnS can shows both type of conductivity (p-type and n-type) and the type of conductivity can be changed by doping percentage of tin [49].

The size of the particles alters the degree of the confinement of the electrons and affects the electronic structure of the solid, especially the band gap edges, which are tunable with particle size. A material achieves special properties when the size of its particles goes to nanoscale range especially the particle diameter range in between 1 nm to 100 nm [50]. Nanoparticles can be categorized in different types, On the basis of their particle size, shape as well as its diverse physical and chemical properties. According to the reduction in dimension of the nanostructured materials, the nanoparticles can be classified into mainly three categories such as 0D structure i.e the system confined in three dimensions, 1D structure i.e the system confined in two dimensions and 2D structure i.e the system confined in one dimension [51]. Nanoparticles are outsized than the atoms and molecules in separately but obviously minor than the bulk solid. Therefore, they do not obey absolute quantum mechanics and pure classical physics perfectly. These two basic differences mainly depend on two factors. Firstly, the nanoparticles possess the high dispersion properties in the solvent. As the particle size of a nanocrystal decreases, the surface to volume ratio (aspect ratio) increases. The second thing is observed in case of metals and semiconductors. The size quantisation effect is noticeable when the size of the nanoparticle is equivalent to wavelength of the electron i.e. the de Broglie wavelength/mean free path of its charge carriers (i.e. electrons and holes). Therefore, the quantum confinement effect of nanoparticles can take place when the size of the particles is comparable to Bohr radius of Exciton [52]. The valance and conduction band edge of the charge carriers are split into discrete as well as quantized electronic levels. This splitting of the band edge of the carriers is due to the spatial confinement. These discrete as well as quantized electronic levels are analogous to the atoms and molecules. It is observed that with decrease in particle size the spacing between the electronic levels as well as band gap energy increases. Hence the interaction between electron hole pairs (i.e. coulomb interaction) cannot be neglected. Therefore, this coulomb interaction

gives an overall superior kinetic energy. An exciton can be treated as quasi-particle which can be formed when Coulomb-interaction between electrons and holes in semiconductor nanoparticles formed a bound pair states. When the light is incident upon the semiconductor nanoparticles, an electron promotes from the valence band to the conduction band of the nanoparticles. As a result, in absence of electron, a positively charged particle i.e hole is created in the valance band [53]. The excitonic Bohr radius of the bounded electron-hole pair can be defined by the following formula:

$$a_0 = \frac{\epsilon h^2}{2\pi \mu e^2}$$

Where, $\mu = \frac{m_e^* m_h^*}{m_e^* + m_h^*}$ is the reduced mass of the nanocrystal, m_e^* is the effective mass of electron, m_h^* is the effective mass of hole, ϵ is the dielectric constant of the material.

In this confinement regime, the optical and electrical properties of the semiconductor nanoparticles are size as well as shape dependent. Therefore, the confinement regime can be classified into three categories such as: strong confinement regime ($a < a_h, a_e$), intermediate confinement regime ($a_h < a < a_e$) and weak confinement regime ($a > a_h, a_e$). Where, a is the critical dimension of nanocrystals, a_h is the critical dimension of hole and a_e is the critical dimension of electron [54]. Tin sulfide (SnS) semiconducting nanoparticles have different applications in vast research areas such as: solar cell [55-56], gas sensor [57], photo detector [58], Li/Na-ion battery [59-60], electrochemical capacitor [61] etc. Different structure of SnS such as nanoparticles, nanorods, nanoflowers, nanosheet, nanowires [62-65] etc. can be synthesized by different process such as solvothermal [63], hydrothermal [64], chemical bath deposition (CBD) [65], physical vapour deposition (PVD) [66], microwave oven assisted synthesis [67], spray pyrolysis [68] as well as wet chemical methods [69].

The current work is to synthesize high quality of SnS nanocrystals by cost effective way. SnS nanoparticles have been prepared by varying the growth conditions, growth

technique as well as reagent ratio. Structural, optical, electrical as well as optoelectronic properties of the prepared good quality SnS nanocrystals have been studied. The current research work have been focused to fabricate different types of devices and to study their different characteristics.

The high quality of SnS nanocrystals are initiated with varying the growth conditions i.e time using chemical reduction method. Temperature and reagent ratio of $SnCl_2.2H_2O/Na_2S$ are varied for growth of SnS using chemical precipitation method. Fe doped SnS and Mn doped SnS have also been prepared by chemical precipitation method. SnS and SnS-Ag nanocomposite are prepared by solvothermal method. Green synthesized SnS nanocrystals are synthesized using Gymnema Sylvestre leaf extract as a capping agent by this simple and cost effective route. The prepared SnS nanostructure materials have been characterized structurally by X-ray diffraction (XRD) and Transmission electron microscopy (TEM). The surface morphology of the grown samples has been characterized by FESEM study. Optical properties of the as prepared samples were characterized through UV-VIS absorption spectroscopy as well as photoluminescence (PL) spectroscopy. The grown nanostructured are applied in ethanol gas sensor, heterojunction solar cells with Si, dye sensitized solar cells using natural dye. The grown nanocrystals are also used to study the molecular interaction of SnS nanomaterials with bovine serum albumin (BSA).

In recent years, the study on the gas sensing mechanism based on metal sulfide nanoparticles is an important chapter in the field of science and technology. The environment became pollutant by the different types of dangerous gases. Besides, these gases can effect on the skin and other organs of human body. Therefore, to save people, animals and our green environment, it is necessary to focus on the gas sensing behaviour of such gases. Various researches are working on the performance of gas sensors [70-71]. The current approaches are to design low cost, good selectivity, excellent sensitivity and better stability gas sensor

and this is an important challenge to the researchers. Therefore, an attempt is taken to design an ethanol gas sensor by the nanofilm of SnS grown from the dispersed SnS nanoparticles on glass. The fabricated device was characterized electrically and its performance of selectivity, sensitivity and stability were also studied. Response time as well as recovery time of the fabricated gas sensing devices was also measured.

In the past decades, the requirement of renewable energy sources is rising to the all people in the world continuously. Therefore, to fabricate low cost, highly efficient as well as environmental friendly photovoltaic devices (PV) is an important challenge to the researchers. Different types of research works on the field of photovoltaic devices (PV) are going on. The main focus of the researchers is to increase the efficiency of the PV devices [72-75]. Basically, the working principle of solar cell is based on the absorption of photons and production of charge carriers within the junction.

SnS is a semiconducting material with band-gap energy close to the band gap energy of silicon. Since the optical absorption coefficient of tin sulfide (SnS) is greater than that of Si, hence the thickness of SnS-based solar cells must be less than crystalline silicon solar cells. The thickness of SnS layer is less than one micrometer and can absorb the entire solar spectrum [76]. It is reported that with silicon crystal we can make efficient solar cell but it is more expansive. CdTe single crystalline based solar cell has efficiency is around 28%. But the growth as well as fabrication cost of this material is much more expensive compared to Si and hence it is not useful in commercial purpose. But tin and sulphur are largly available in the nature and they are cost effective. Different types of semiconducting materials like CdTe, CdS, CdSe, $CuInGaSe_2$ etc. are used to design photovoltaic devices [77-79]. The amount of Te and In are limited in nature. On the other hand Cd and Se are toxic in the CdTe, CdS, CdSe, $CuInGaSe_2$ solar cell. Copper zinc tin sulfide (CZTS) is earth-abundant essentials, but it is complicated to fabricate solar cell due to its complex composition. This limitation could

be overcome with another absorbing material like SnS. Tin sulfide (SnS) is a new promising material due to its chemical, physical, electrical properties and vast area in optoelectronic and photovoltaic applications. SnS is stable in the presence of H_2O and O_2. Hence tin sulfide has better stability than organic solar cells which are damaged by O_2 and H_2O [76]. Besides, the compositions of SnS are non-toxic, whereas other thin film cells are toxic such as cadmium (Cd), tellurium (Te), selenium (Se) and lead (Pb) [80-81]. On the other hand, the major drawbacks of this inorganic semiconductor are their light absorbing ability in the visible region. To increase the light trapping ability technique of the semiconductor as well as to increase the efficiency of solar cell without increasing the thickness of the active layer we are acquiring a new process using noble metal nano-particles (MNPs) embed in any semiconducting nanoparticles (SNPs). When the electromagnetic waves are allowed to travel along the metal and semiconductor interface then Localized Surface Plasmon Resonance (LSPR) is taking place [82]. This phenomenon mainly depends on size and shape of metal nanoparticles [83]. Maximum number of metal nanoparticles such as Ag, Au, Al etc. shows absorption peak in visible region. Out of all these metal nanoparticles Ag shows best surface plasmon resonance (SPR). The emissions of SNPs increases in presence of MNPs. Solar cells in which metal nano-clusters are used are called plasmonic solar cells. Hence, the current strategy is to fabricate SnS/Si and SnS: Ag/Si heterojunction solar cells. Dispersed SnS NPs and SnS-Ag nanocomposite are deposited by a spin coater on n-Si wafer to fabricate heterojunction solar cell. The fabricated device was characterized electrically through J-V study under dark and illumination. The open circuit voltage, short circuit current, fill factor and efficiency of the fabricated heterojunction solar cells were estimated.

In recent times, it is observed that the demand for renewable energy in the world is increasing rapidly. But, the supply of non renewable energy is not adequate to make up with the rising demand of energy in a tenable way. Therefore, the peoples are searching renewable

energy sources to maintain communal and financial development in the world. There are different types of renewable energy sources in the natural world such as water power, wind power, biofuel, tide, sunshine flux, terrestrial heat etc. But, due to some drawback, these renewable energies are unable to reach to all the peoples in the world. For this purpose, solar energy is the most valuable and ideal energy source. Hence, the solar energy can be considered as the alternate solution for clean, abundant, and renewable energy sources. Photovoltaic (PV) solar cells can convert directly the visible light energy into electrical energy. The current strategy is to construct low cost photovoltaic devices (PV) and to amplify its power conversion efficiency [84-86].

Dye sensitized solar cell is a promising device compared to Si based solar cells due to their easy, low cost of production and therefore high photon conversion efficiencies [87-89]. Generally, researchers have been used TiO_2 as anode material and costly platinum (Pt) electrode as a counter electrode for the fabrication of dye sensitized solar cells [90]. For the fabrication of DSSCs, our main focus on to improve the electron transfer as well as the reduction of recombination rate. So one can be used any other semiconducting materials as a photo anode instead of TiO_2. On the other hand, costly Pt can be replaced by the other less expansive materials as a counter electrode for the fabrication of DSSCs [91-92]. In this regard we have used SnS nanoparticles as photo anode whereas graphite paste was used as counter electrode materials. For these purpose, pure SnS, Fe doped SnS and Mn doped SnS nanoparticles based natural dye sensitized solar cells have been fabricated. Dye sensitized solar cells based on green synthesized SnS nanoparticles have been also fabricated. Acalypha Wilkesiana leaf extract was used as the natural dye as a photosensitizer. The grown devices are characterized by electrically through J-V study. A comparative study of the efficiencies of the fabricated dye sensitized solar cells has been analysed.

The study of semiconductor nanoparticles (NPs) in the biological labelling is an enormous interest in the field of biophysics and technology [93-95]. The biological phenomenon include the long PL decay lifetime, large quantum efficiency, fine emission (PL) spectra, high performance of photo stability and continuous optical absorption spectra (UV-vis) are the crucial factors for the diagnostics and the inflection of cell activity. To identify the biological function on the basis of physical experience, we have studied the interaction as well as the formation of bioconjugate of bovine serum albumin (BSA) with SnS nanoparticles. The HRTEM images, optical absorption spectra as well as fluorescence quenching phenomenon are employed to investigate the BSA-SnS NPs interaction and the structural modification of bovine serum albumin (BSA) in the presence of SnS NPs.

The main objective of my thesis is to synthesize SnS and doped SnS nanocrystals by cost effective method. Green synthesized SnS nanoparticles have been also prepared. We have synthesized different sizes of the nanocrystals by changing the growth conditions, growth technique as well as reagent ratio of tin chloride dihydrate and sodium sulfide. The as grown samples were characterized by structurally, optically as well as electrically. The SnS nanostructures have been applied in different types of devices as like as ethanol gas sensor, heterojunction solar cell with Si, dye sensitized solar cell using natural dye. Also the molecular interaction of SnS nanocrystals with bovine serum albumin (BSA) was studied.

1.2. Literature Review

1.2.1. Synthesis technique and characterization

S. Suresh et al. [96] synthesized tin sulfide nanoparticles (SnS) through wet chemical method at room temperature. The as prepared sample was characterized by XRD, FESEM, TEM and optical absorption spectroscopy. The orthorhombic phase of SnS nanoparticles were confirmed by XRD. Spherical nature of SnS nanoparticles were obtained from TEM image and the average diameter of the particles were 15 nm. From optical absorption study, the band gap of the of the SnS nanoparticles was close to 1.8 eV.

S. Sohila and his groups [97] prepared SnS nanosheets via wet chemical method. Ethylene glycol was used as a reaction medium. Structural, morphological and optical properties of the prepared SnS nanosheets were characterized by X-ray diffraction (XRD), high resolution transmission electron microscope (HRTEM), UV-VIS-NIR absorption spectroscopy and photoluminescence spectroscopy (PL). XRD results showed the orthorhombic crystal phase of SnS and no others impurities were detected. They reported that quantum confinement effect is mainly responsible for the blue shift of SnS nanosheets. PL spectra exhibits that two emission spectra with corresponding band gaps are 1.75 and 1.57 eV respectively which are due to defect state transitions.
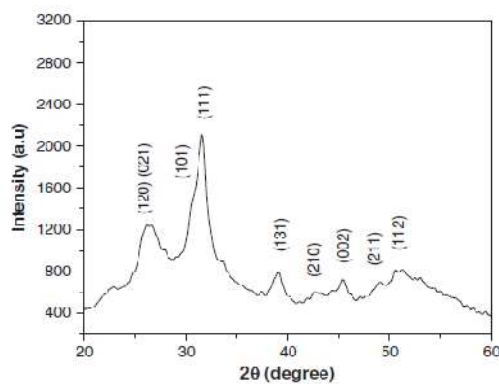
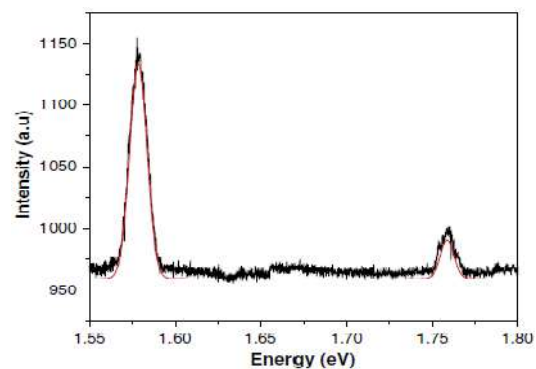**Fig. 1.1.** Powder XRD pattern of SnS nanosheets   **Fig. 1.2.** Room temperature photoluminescence spectrum of SnS nanosheets. The colored solid curve is a Gaussian fit to the data. [97]

X. Gou et al. [98] prepared good quality SnS from $SnCl_2 \cdot 2H_2O$ and thioacetamide (TAA) through precipitation method at 60 ^0C .The as-prepared SnS samples were characterized XRD, FESEM, TEM, HRTEM and Raman spectroscopy. XRD result confirmed that all the planes are exactly matched with orthorhombic crystal phase of SnS. From Raman spectra they reported that, there are two individual peaks which are situated at 189 and 220 cm^{-1}respectively. These Raman peaks correspond to A_g mode of SnS crystal. Multilayer nanostructure of SnS was obtained and the average diameter of the particles was in the range of 30–100 nm.
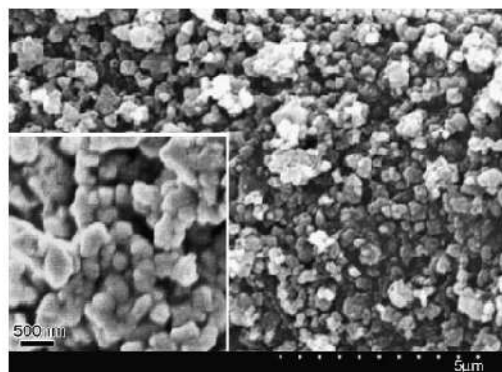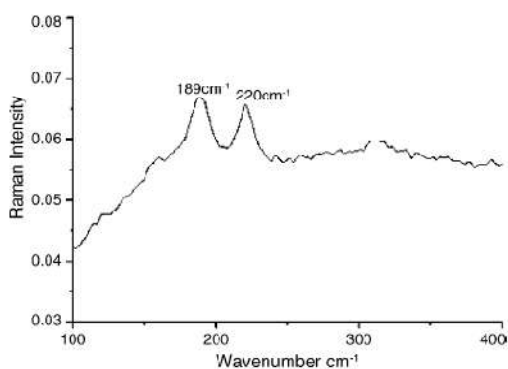

Fig. 1.3. Raman spectrum of the as-prepared SnS nanoparticles at room temperature [98]

Fig. 1.4. SEM micrograph of the as-synthesized SnS nanoparticles. The inset is the SEM image detailing a region of the nanoparticles. [98]

M. Pal et al. [99] synthesized SnS through nonaqueous chemical route in the presence of different amounts of triethanolamine (TEA) used as a complexing agent. The grown nanoparticles were studied by X-ray diffraction, high resolution transmission electron microscopy, Energy-dispersive X-ray spectroscopy, micro Raman and optical absorption spectroscopy. The average size of the nanocrystals was found to be approximately 10 nm that is confirmed by HRTEM. They reported that the crystal size decrease gradually with the increase of the amount of triethanolamine (TEA). EDS analysis confirmed that, in case of TEA free sample the stoichiometric is maintained well whereas for TEA capped SnS, the

atomic percentage of sulphur is a little higher than tin. They showed that the as prepared SnS nanoparticles are a good absorber in the visible and NIR spectral range. They determined the direct as well as indirect band gap of the sample was found to be 1.74 and 1.2 eV respectively. They also reported that the values of band gap energies moved to the higher energy side with raising the quantity of TEA.
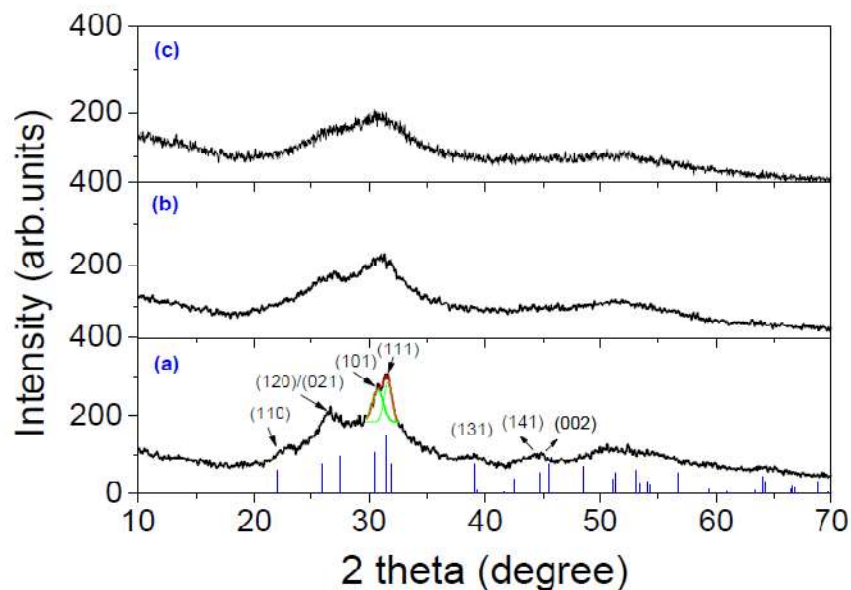

Fig.1.5. X ray diffraction patterns of SnS nanoparticles synthesized with: (a) 0 ml,(b) 2 ml and (c) 4 ml of TEA. [99]
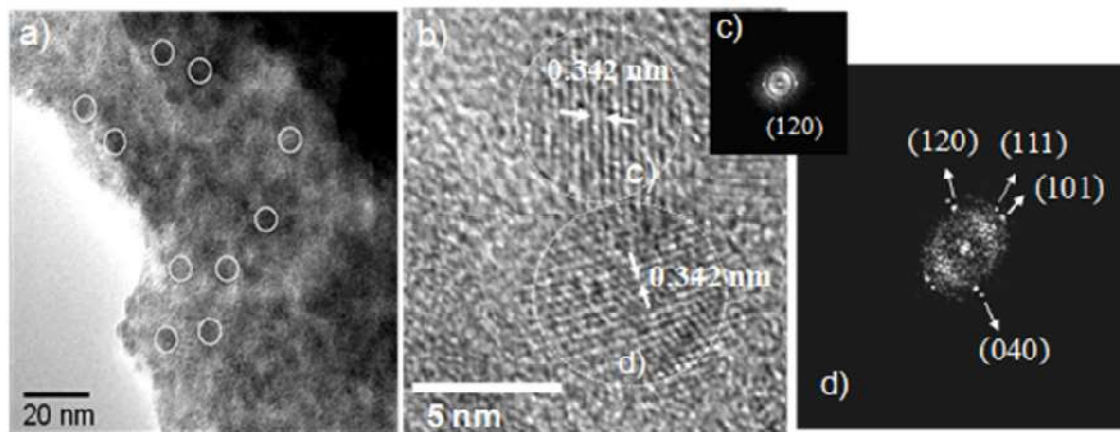

Fig. 1.6. TEM (a) and HRTEM (b) images of SnS nanocrystals grown in absence of TEA. FFT patterns of the area enclosed in the circular frames of the same HRTEM image is shown in figures (c) and (d) [99].

S. H. Chaki et al. [100] synthesized and characterized of different morphology of SnS nanomaterials. They reported the orthorhombic phase of XRD pattern of SnS nanostructued. The Raman spectra associated with three peaks are situated at 98 ± 1, 224 ± 4 and 302 ± 1 cm^{-1}. Different nanostructured of SnS i.e. particles, whiskers and ribbons were confirmed by TEM analysis. Optical absorption study indicates that these SnS nanostructured possess a large optical absorption coefficient in the visible region. Direct as well as indirect optical band gap of the various SnS nanostructured were determined. The electrical properties of the different SnS nanostructured were studied. They reported the values of activation energy vary from 0.15 eV to 0.29 eV, Hall coefficient vary from 1.25×10^6 cm^3 C^{-1} to 12.02×10^6 cm^3 C^{-1} and Hall mobility vary from 18.74 cm^2 V^{-1} sec^{-1} to 115.09 cm^2 V^{-1} sec^{-1}. The sign of Hall coefficient indicates the p-type character of the as-prepared SnS nanostructured.
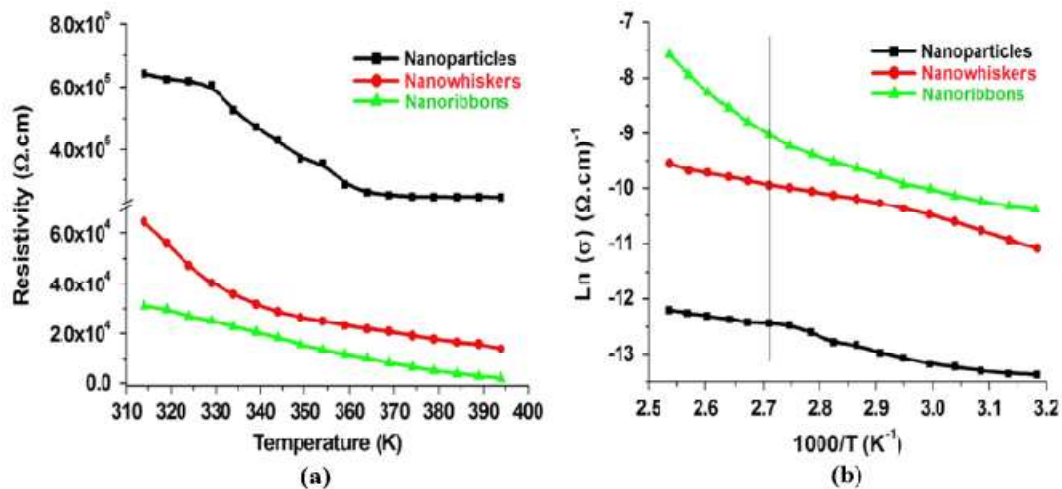

Fig.1.7. Plots of (a) electrical resistivity versus temperature and (b) Ln(σ) versus 1000 T^{-1}.[100]

J. Henry et al. [101] prepared SnS nanoparticles by simple precipitation method through $SnCl_2.2H_2O$ and $Na_2S.xH_2O$. They have studied the structural and optical properties of SnS nanoparticles. XRD pattern confirm the Herzenbergite orthorhombic phase of SnS nanoparticles. They have prepared SnS thin film by the technique of electron beam

evaporation at room temperature as well as annealed temperature of 100 ^{0}C, 200 ^{0}C and 300 ^{0}C. The structural and optical properties of the SnS nanofilms were carried out through XRD and UV-Vis spectroscopy. They found that the optical band gap of SnS films were reduced from 1.77 to 1.57 eV with the increase of annealed temperature.

H. Kafashan et al. [102] reported the effect of Al doping SnS on the structural and optical properties. The structural and optical properties of deposited thin films were analysed by XRD, FESEM, UV-vis and PL spectroscopy. All the diffraction planes are perfectly matched with the orthorhombic crystal structure of SnS that was confirmed by XRD analysis. The crystalline nature of the Al doped SnS increased with increasing of the amount of Al concentration. The optical absorption coefficient of Al-doped SnS film was greater than 10^{4} cm^{-1}. So they reported that the films are good absorbing for sunlight throughout the entire range of solar spectrum. They have found that the band gap decreased from 1.31 to 1.20 eV with increase of Al doping. The PL spectra showed a red shift with increasing of Al concentration. Therefore, they concluded that the Al doping takes an important role to modify the optical and morphological properties of Al-doped SnS thin films.
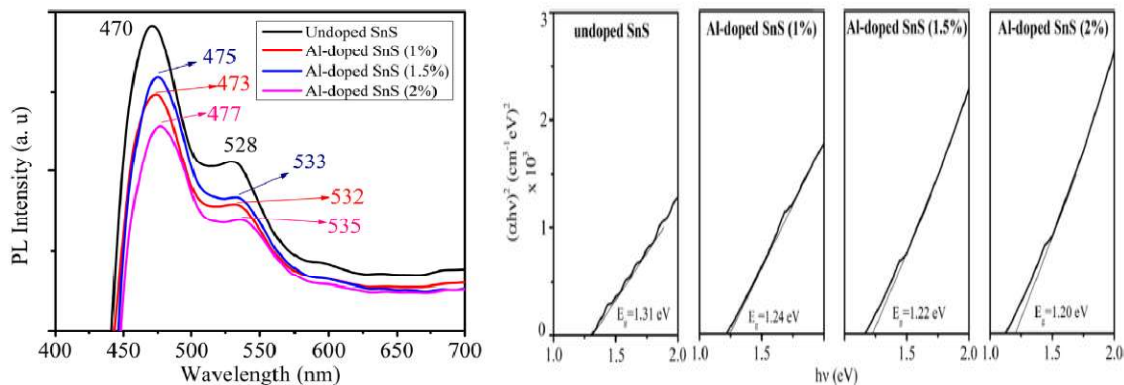

Fig. 1.8. PL spectra of undoped SnS and Al-doped SnS films with different Al-doping concentration. [102]

Fig. 1.9. Variation of (αhυ)^{2}with for undoped SnS and Al-doped SnS at different Al-doping concentrations.[102]

H. Kafashan et al [103] prepared pure SnS and In-doped SnS thin films by electrochemical route. The as-prepared SnS and indium doped SnS thin film were

characterized structurally through X-ray diffraction, field emission scanning electron microscopy, energy dispersive X-ray analysis, atomic force microscopy, transmission electron microscopy and optical characterization through photoluminescence study. XRD analysis established that pure SnS and In-doped SnS are crystalline in nature and belongs to the orthorhombic crystal structure. Particles nature is in spherical shape that was confirmed by TEM image. The crystallite size of pure SnS and In-doped SnS were determined with the help of Scherrer's and W-H method. PL spectra of nondoped SnS and Indium doped SnS thin films containing two emission spectra which are situated at 482 nm and 559 nm.
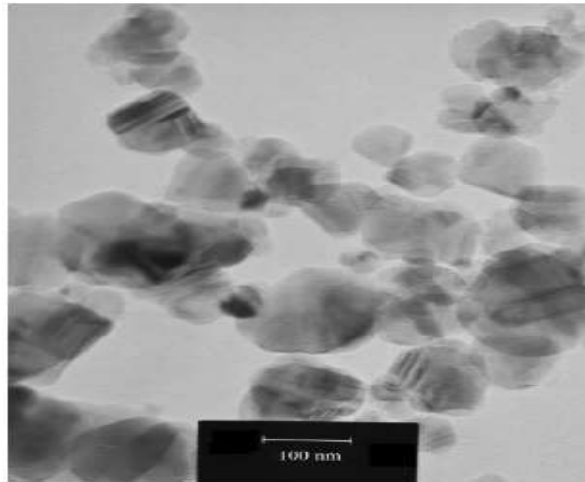

Fig. 1.10. TEM image of undoped SnS [103]

M. Reghima and his coworkers [104] followed chemical bath deposition method to synthesize Fe doped SnS nanofilm with different Fe concentration. The structural, optical and electrical properties of the prepared Fe-SnS thin films were studied through X ray diffraction (XRD), atomic force microscopy (AFM), field emission scanning electron microscopy (FESEM) and thermally stimulated current (TCS). The experimental results show that Fe doping takes a vital role in the physical properties. They found that the Fe doped samples is a good crystalline when the doping percentage of Fe was 8%. TEM image reveals that 24 nm is the largest particle size. The doping of Fe affects the surface roughness. For pure SnS the

value of surface roughness was about 64 nm whereas for Fe doped SnS it was about 40 nm. The presence of Fe was confirmed by EDAX analysis. Optical absorption study suggests the decrease in band gap of Fe doped SnS compared to undoped SnS thin film. They also calculated the activation energy of trapping levels of pure and Fe-doped SnS thin films. An interesting phenomenon was observed when the doping concentration of Fe was 4% and 8%. In this two doping concentrations, the existence of numerous traps was confirmed by the double values of the activation energy.

B. Thangaraju [105] et al. prepared SnS/ glass thin film at 350 ^{0}C, SnS2/ glass and SnS2/ FTO thin films at 275 ^{0}C by the spray pyrolysis process. XRD results suggest that SnS thin film was in amorphous in nature but polycrystalline nature were found to be in case of SnS_2 thin films. The average crystal diameter of SnS_2/glass was 115 Å whereas SnS_2/ FTO were 324 Å. From optical properties, a direct band gap of 2.44 eV for SnS_2 thin films and an indirect band gap of 1 eV for SnS thin films were exhibited. Optical properties also exhibits that SnS and SnS_2 are both good absorber material in solar spectrum. The experimented absorption coefficients of SnS_2 and SnS thin films in the visible spectrum were close to 2×10^4 cm^{-1} and 4.6×10^3 cm^{-1}. They found that the as-prepared thin films are n-type in electrical conductivity. The reported values of conductivities of SnS thin films in dark as well as under light were found to be $\sigma = 2 \times 10^{-3}$ ohm^{-1} cm^{-1} and $\sigma = 2.45 \times 10^{-2}$ ohm^{-1} cm^{-1} respectively.

N. K. Reddy and his groups [106] reported that SnS films were prepared by spray pyrolysis method. Corning 7059 glass were employed to deposit SnS thin film in the temperature range of 100 ^{0}C to 450 ^{0}C. The deposited SnS films have been studied by its electrical properties. Different types of electrical parameters such as electrical conductivity, Hall mobility, activation energy and carrier concentrations were determined from the electrical behaviour of SnS thin films. They reported that the type of electrical conductivity

mainly depends on film grown temperature (T_s). They observed that the films show n-type conductivity when $T_s < 300\ ^0C$ and $T_s > 375\ ^0C$. Besides, the films show p-type conductivity at the range of mid temperature i.e. at $300\ ^0C < T_s < 375\ ^0C$. The electrical resistivity of the grown SnS films was varied from 300 ohm-cm to 10^{-1} ohm-cm. They observed that the electrical resistivity decreases quickly when the substrate temperature (T_s) varies from $100\ ^0C$ to $275\ ^0C$ and exhibits almost constant electrical resistivity (~30 ohm-cm) when the range of substrate temperature was $300\ ^0C$ to $375\ ^0C$. The electrical carrier concentrations increase with the rinsing of substrate temperature. The carrier density reached a higher value (10^{17} cm$^-$^{3}) when substrate temperature arrived at $450\ ^0C$ whereas films show a net charge density of 10^{15} cm^{-3} in the range of temperature $300\ ^0C$ to $375\ ^0C$. The growth of hall mobility were observed and arrived at the maximum value of 140 cm^2 / V s when substrate temperature was reached to $400\ ^0C$. The temperature dependent of activation energies were also evaluated. The calculated values of activation energies were found to be 0.46 eV and 0.35 eV for 0.3 µm and 0.6 µm thickness of SnS films respectively.

S.S. Hegde et al. [107] demonstrated physical vapor deposition process to synthesized tin sulfide (SnS) single crystal. Structural, optical and electrical properties of the grown SnS single crystal were studied through appropriate techniques. A good stoichiometric ratio (1.02) was maintained for the single crystal of SnS which was confirmed by EDAX analysis. Layered type growth mechanism has been observed by SEM study. AFM study revealed that crystal surface roughness was very low and it was found to be 0.22 nm. Orthorhombic crystal structure with (0 4 0) orientation were confirmed by XRD measurements. Direct and indirect optical band gap have been calculated from optical absorption spectra. Electrical measurements of SnS single crystal include the type of conductivity, electrical resistivity, carrier concentration as well as activation energy. They reported that the as grown crystals were of p-type in nature. The electrical conductivity of the grown SnS single crystal was

measure in the temperature range 115-300 K. The reported electrical resistivities, carrier concentration of the prepared SnS single crystal were found to be 120 ohm-cm and 1.52×10^{15} cm^{-3} respectively.

Table: 1.1

Results obtained from the resistivity and Hall effect measurements of SnS crystals at room temperature [107]

Parameters	Values
Resistivity ρ (ohm-cm)	120.35
Hall coefficient R_H (cm^3 coloumb^{-1})	4108.9
Type of conductivity	p-type
Mobility μ_H (cm^2 Vs)	34.14
Carrier concentration η (cm^{-3})	1.52×10^{15}

Priyal Jain et al. [108] reported that the SnS:Ag nanocomposite thin films were developed by thermal evaporation in a vacuum under the pressure of 4–5 10^{-5} Torr. The as grown thin films were characterized experimentally by XRD, optical absorption, XPS, SEM and SAED. XRD measurements have been studied with the variation of thickness of SnS:Ag nanocomposite thin films. They found that all the films are in polycrystalline in nature associated with the orthorhombic crystal structure of SnS. Scherrers formula was used to calculate the crystal size of SnS and Ag nano-particles. It was noticed that there was a linear increment of grain size with the increment of film thickness. The average grain size of SnS: Ag nanocomposite films were approximately 12 nm with the film thickness below 600 nm, but the grain size was in the order of 32–42 nm for higher thickness nanocomposite films. From optical absorption spectra, it was found that there are two peaks situated at 500 nm and 580 nm. These two peaks have been treated as longitudinal mode (LM) and transverse mode (TM). The Localized Surface Plasmon Resonance (LSPR) due to the silver (Ag) nano-

particles. All these experimental results have been also considered as theoretically using various computational models.

S. Sohila and his co-workers [109] synthesized SnS nanorods and SnS/ZnO nanocomposite by simple chemical method. Structural and optical properties of the prepared samples were studied through XRD, TEM, Raman, EDAX and UV-vis absorption spectroscopy. They reported the orthorhombic crystal phase of SnS nanorods but orthorhombic and wurtzite structure both are obtained in SnS/ZnO nanocomposite that was confirmed by XRD study. No impurity peaks were observed XRD image. From TEM image they exhibited that the average diameter of SnS NRs was found to be 85 nm and length was few micrometers whereas approximately 12 nm average particle size was obtained in SnS/ZnO nanocomposite. Direct and indirect band gap of SnS nanorods have been calculated from optical absorption spectra and it were found to be 1.35 and 1.21 eV respectively.

E. Turan et al. [110] focussed on chemical bath deposition process to form SnS thin films. Structural and optical properties have been examined by different techniques. An orthorhombic-herzenbergite crystal structure with lattice parameters a = 4.39 Å, b = 11.17 Å, c = 3.97 Å was obtained from XRD measurements. Crystal size has been determined from Scherrer formula and it was found to be 67 nm. Atomic ratio of Sn/S was 49.8: 50.2 and it was confirmed by EDAX analysis. The optical properties of the sample have been studied in the range of wavelength 190 to 3300 nm. The optical direct band gap of the deposited SnS thin films has been calculated from transmission spectra. The value of the optical band gap was 1.31 eV. Various types of optical parameters of the SnS films such as optical constants (n, k, ε), plasma frequency (ω_p), carrier concentration, N_{opt} have been also calculated from the transmittance spectra. They reported that at high frequency the refractive index of SnS films was almost constant and it was found to be 1.84.

E. Guneri et al. [111] prepared SnS thin films through chemical bath deposition process as a function of deposition times (2-10 hours) at the temperature of 60 ^{0}C. They reported that the deposition time effected on the properties of structural, microparameters, surface morphology, optical and electrical of tin sulfide thin films. The deposited thin films were investigated through XRD, SEM, EDX and UV-vis absorption spectroscopy. XRD results confirmed that the SnS films possessed an orthorhombic crystal phase. The average particle size has been increased from 22 nm to 24 nm with the increase of deposition time from 2 h to 6 h and after that it decreased to 22 nm. Chemical compositions of the deposited SnS thin films were determined from EDX analysis. The reported value of the atomic ratio of Sn:S was approximately 1.49. From optical absorption study they found the allowed direct band gap (1.30–1.97 eV), allowed indirect band gap (0.83–1.36 eV), forbidden direct band gap (0.93–1.49 eV) and forbidden indirect band gap (0.62–1.23 eV) of the deposited SnS thin films. Electrical parameters such as type of conductivity and hall resistivity were determined from Hall Effect study. They reported that the deposited films were p-type in nature and the value of resistivity of the films has changed with deposition time.

K. S. Kumar [112] reported the effect of antimony (Sb) doping concentration on the crystal structural, optical as well as electrical properties of tin sulfide thin films prepared by spray pyrolysis methodology. XRD study found that the SnS and SnS:Sb thin films were in the orthorhombic crystal phase with the orientation in direction of (111). The SnS:Sb thin films showed a good crystalline material up to 6 at.% of Sb doping concentration but above 6 at.% of Sb doping, the crystalline quality and the favourable direction was destroyed. Optical properties have been studied through UV-vis absorption spectra and found that the optical band gap decreased with increase of doping percentage. The reported value of the optical bang gap lies in between 1.60 eV to 1.15 eV. PL measurements have been done and emission spectra were observed at 760 nm for all thin films. From electrical measurements they

reported the value of lowest electrical resistivity of 2.598×10^{-2} ohm-cm, higher carrier concentration and higher mobility of 684.42 cm^2 /V s of the deposited thin films when Sb doping concentration was 6 at.% .

A. E. Oluwalaney et al. [113] reported the temperature and capping agent effects on structural, morphological and optical properties of SnS nanocrystals. Oleic acid (OA) and octadecylamine (ODA) were used as capping agent. SnS nanocrystals were prepared in different temperatures i.e. at 150 ^{0}C, 190 ^{0}C, and 230 ^{0}C. The as prepared OA and ODA capped SnS nanoparticles were investigated through XRD, TEM, EDAX, and UV-VIS spectroscopy. They reported the orthorhombic crystal structure of the OASnS and ODASnS nanoparticles. TEM results showed the spherical shaped and cubic shaped nanocrystals were obtained in OASnS and ODASnS respectively. Smallest sized nanocrystals (10.67–17.74 nm) were achieved at 150°C for OASnS whereas the biggest-sized nanocrystals (67.04–80.15 nm) were found at 230° C for ODASnS. The presence of Sn and S in the synthesized SnS nanocrystals was confirmed by EDAX analysis. Optical absorption has been studied through UV-VIS spectroscopy in the optical range 300-800 nm. They determined the optical direct band gap from the optical absorption study. The reported band gaps were found to be 1.71–1.95 eV and 1.93–2.81 eV for OASnS and ODASnS nanoparticles respectively.
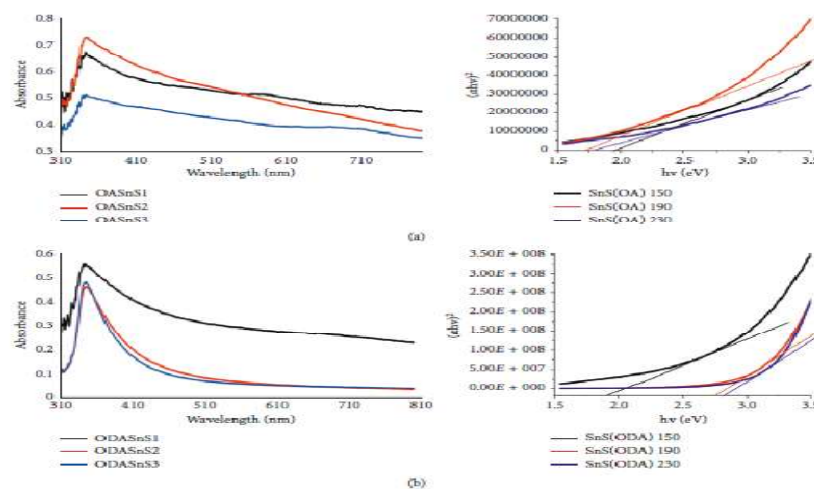

Fig. 1.11. UV-Vis absorption spectra of OASnS with its Tauc plot (a) and ODASnS with its Tauc plot (b).[113]

S. Rabaoui et al. [114] synthesized Cu_2SnS_3 (CTS) nanoparticles at 200 ^{0}C for 24 hours through solvothermal technique. The as prepared nanoparticles were characterized structurally, optically and electrically by XRD, TEM and UV-vis absorption study. XRD results reported the cubic phase of CTS nanoparticles with a crystal size in the range of 11 nm to 15 nm. From TEM image they found the good crystalline behaviour of the prepared sample and possess the crystal size in between 10 nm to 19 nm which tallies the XRD result. Optical measurement has been taken in the UV to visible optical range (200 nm to 1000 nm). The calculated direct band gap of the prepared CTS nanoparticles was found to be 1.27 eV. The ac conductivity versus frequency in different temperatures of the Cu_2SnS_3 nanoparticles was measured.

H. Zhu and his groups [115] prepared SnS nanoflowers with the assistance of thioglycollic acid through hydrothermal technique at 250 °C. The as prepared sample was studied and investigated by X-ray diffraction (XRD), scanning electron microscopy (SEM), EDAX and UV-vis absorption spectroscopy. XRD result shows that all diffraction planes are perfectly matched with orthorhombic crystal of SnS with lattice constants a= 3.99 Å, b= 4.34 Å and c= 11.2 Å. Scherrer's formula have been employed to determine the particle size and it was found to 60 nm. Surface morphology was studied by SEM analysis and flower-like SnS nanostructures were obtained. The chemical composition of SnS was obtained by EDAX measurements and the atomic ratio of Sn/S was found 1:1 and this result confirmed that the stoichiometric ratio of SnS nanoflower was well maintained. The optical band gaps were measured through UV-vis absorption spectrum. The direct and indirect band gaps of the SnS nanoflowers were evaluated and it was found to be 1.53 and 1.43 eV respectively.

P. R. Bommireddy et al. [116] reported structural, optical as well as electrical properties of the prepared Cu doped SnS thin films. The Cu-SnS thin films were deposited in different concentrations (0-8%) of Cu. XRD study exhibited that all the deposited Cu-SnS

thin films were polycrystalline in nature. All the diffraction peaks indexed the orthorhombic structure of SnS with the favoured (111) direction. The XRD spectra also revealed the improvement of preferential direction as well as crystalline quality of Cu-SnS thin films up to 4% Cu doping concentration while the preferential direction and crystalline quality were destroyed when the doping concentrations of Cu was above 4%. The optical band gaps were calculated from the transmission spectra. They found that the optical band gap decreased from 1.46 eV for pure SnS to 1.37 eV for 4% Cu-doped SnS. Electrical characterization were analysed through hall measurements. They reported that the SnS thin films are p-type in nature. They also reported that the electrical resistivity decreased from 10^5 Ω-cm (pure SnS) to 10^3 Ω-cm (4% Cu doped SnS).

H. Kafashan [117] el al. prepared SnS thin films in various deposition potentials and solution concentrations through electrodeposition process. Tin chloride ($SnCl_2$) and Sodium thiosulfate ($Na_2S_2O_3$) were used as the source of tin and sulphur respectively. FTO coated glass were used as substrate. The electrodeposited films were characterized and studied by X-ray diffraction, field-emission scanning electron microscopy, photoluminescence and ultraviolet–visible spectroscopy. The X-ray diffraction patterns revealed that the deposited SnS films are orthorhombic crystal structure. They found that the morphology of the films was remarkable changed with the variation of deposition potential and bath concentration. EDAX study investigated the atomic ratio of Sn/S. The electro deposition potential were varied from -0.6 V to -1.2 V. The variations of bath condition and electro deposition potential affect the band-gap of that material. The photoluminescence spectra of the SnS films showed two peaks which one in the visible region and another one in the infrared region. From UV–Vis spectra, they reported that the band gap energy changes from 1.21 to 1.44 eV.

V. S. R. R. Pullabhotla et al. [118] synthesized high quality SnS nanoparticles using Tetrathiourea tin (II) chloride. The as prepared SnS nanoparticles were investigated and

studied by X-ray diffraction (XRD), transmission electron microscopy (TEM), high resolution transmission electron microscopy (HRTEM), SEM-EDX and UV-Vis-NIR. The high quality SnS nanoparticles were orthorhombic crystal structure. TEM study revealed that various types of morphologies and particle size were obtained. The average grain size of SnS nanoparticles was found to be 52.86 nm. EDAX analysis confirmed that there were no impurity elements in the SnS sample. The lattice spacing of the SnS nanocrystals were calculated from HRTEM image and found to be 0.29 and 0.39 nm, which can be assigned as (101) and (120) diffraction planes. Optical absorption measurements have been studied for the high quality SnS nanoparticles displayed both the direct as well as indirect band gap energy close to 1.77 eV and 1.52 eV respectively.

H. Kafashan et al. [119] prepared In doped SnS thin films via electrodeposition technique on the substrate of fluorine coated tin oxide (FTO). The as prepared SnS:In thin films were characterized structurally and optically though different tools and techniques. $SnCl_2$ and $Na_2S_2O_3$ have been used as the chemical reagents. The XRD analysis signified that all the In doped SnS thin films were orthorhombic structure with polycrystalline in nature. The value pH, temperature of bath, time of deposition and deposition potential were maintained at 2.1, 60 ℃, 30 minutes and -1 V respectively. From FESEM images, they reported that a change in morphology was observed with the increase in In-doping percentage. The variation of optical absorption coefficient of SnS:In thin films has been studied through UV-Vis measurements. The direct band gap was calculated and was found to 1.40-1.66 eV. The photoluminescence spectra of pure SnS contained four emission peaks consist of a UV emission peak, two blue emission peaks and an IR emission peak.

M. Gurubhaskar et al. [120] reported a facile, simple, cost effective and surfactant free (TGA) hydrothermal synthesis route to synthesize SnS nanoparticles. Stannous chloride dehydrates and thiourea was taken as starting material. The autoclave was maintained at

different reaction temperature 100 ^{0}C, 130 ^{0}C, 160 ^{0}C and 19 ^{0}C for 6 hours. The effects of reaction temperature on structural and optical properties have been studied using XRD, FESEM-EDAX, TEM and UV-Vis measurements. The XRD results investigated that the as prepared SnS nanocrystals are orthorhombic crystals phase with favourable (040) crystal plane. From TEM results they reported that smallest crystal size (3 nm to 5 nm) of SnS was obtained at 160^{0}C reaction temperature. They found that the reaction temperature also affects on the surface morphology. Different types of surface morphology such as nanoflowers, nanoflakes, spherical particles and nanogranuels were obtained. The chemical compositions of the as-synthesized SnS nanoparticles were studied using EDAX analysis. Optical absorption measurement have been analysed and determined the direct and indirect band gap energies were found to be 1.5 eV and 1.19 eV of SnS nanoparticles growth at 160 ^{0}C.
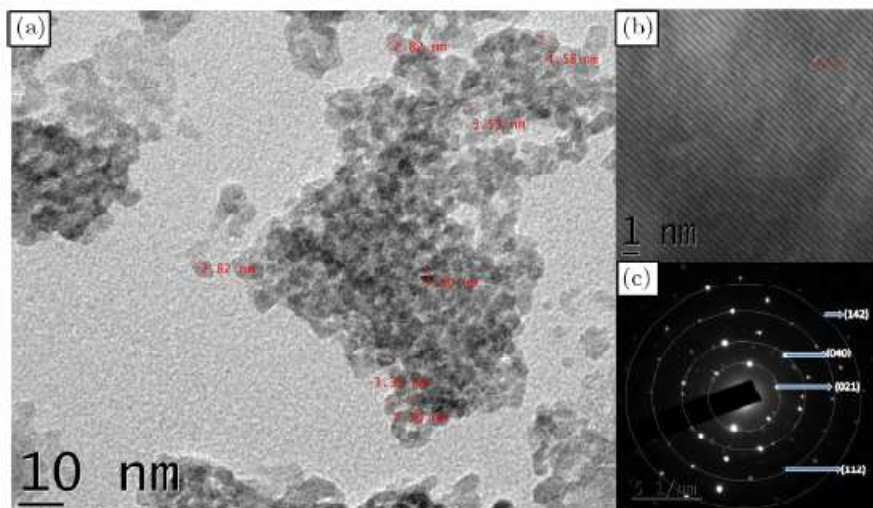

Fig. 1.12. (a) TEM image (b) HRTEM and (c) SEAD images of as-synthesized hydrothermal SnS nanoparticles at reaction temperature 160 ^{0}C. [120]

G. G. Guillen et al. [121] synthesized SnS nanoparticles through different liquid medium (Distilled water, Acetone, Ethanol, 2-Propanol) via pulsed laser ablation technique. A Nd:YAG laser having wavelengths 532 and 1064 nm with a pulsed of 10 ns, 10 Hz has been employed for this purpose. The structural, chemical and optical properties of the as prepared samples were investigated through XRD, TEM, XPS, UV-Vis and PL study. From

XRD study they reported that SnS nanoparticles are well crystalline orthorhombic structure. The chemical state were analysed through XPS study. They also reported that the optical band gap energy of as synthesized SnS colloidal nanoparticles shifted towards the higher energy side due to the increased in fluence energy. The PL measurements of SnS nanocolloids confirmed that the emissions are fall in the visible range.

Table: 1.2

Summarization table of results for SnS nanoparticles obtained by pulsed laser ablation in liquid [121]

Ablation wavelength (nm)	Liquid medium	Energy fluence (J/cm^2)	Average size (nm)	Band gap (eV)	Emission peak (nm)
532	Distilled water	6	39	2.1	487, 545
		24.8	23	2.5	487, 545
	Acetone	6	5	2.7	487, 546
		24.8	5	2.7	487, 546
	Ethanol	6	18	2.6	487, 546
		24.8	21	2.8	487, 546
	2-Propanol	6	29	2.2	487, 546
		24.8	28	2.2	487, 546
1064	Distilled water	6	25	1.6	427, 493, 529
		24.8	28	1.8	427, 493, 519
	Acetone	8.7	-	1.8	488, 545–548
		30	17	2	488, 545–548
	Ethanol	8.7	-	1.7	487, 546
		30	-	2	487, 546
	2-Propanol	8.7	23	1.6	487, 542
		30	21	2.3	487, 542

M. M. Rao et al. [122] synthesized SnS nanoparticles and SnS nanorods via simple hydrothermal process. $SnCl_2.2H_2O$ and thiourea aqueous solution was used as chemical reagent. The solutions were placed in an autoclave. The reaction was maintained at 180 ^{0}C for 2 and 8 hours respectively. The as prepared samples were characterized structurally through XRD and TEM. The XRD images of SnS NRs and SnS NPs can be considered as orthorhombic crystal phase of SnS. No impurity peaks were detected in XRD images. From TEM study, they reported that the length of SnS NRs was found 55–250 nm and the diameter was varied from 10 to 50 nm. Besides, the crystal size of SnS NPs lies in the range of 3–10 nm.

W. A. A. Syed et al. [123] investigated that the SnS nanoparticles were synthesized by precipitation method at a reaction temperature of 250 ^{0}C for 20 hours. The as synthesized SnS nanoparticles were investigated structurally by XRD, SEM and optically by DRS, FTIR. The as grown SnS anoparticles are orthorhombic crystal phase was confirmed by XRD pattern. The grain size was determined with the help of Debye-Scherrer formula and found to be 48.44 nm. A uniform spherical surface structure was studied through SEM analysis. The direct as well as indirect band gap energy was determined from DRS spectra with the help of Kubelka-Munk function. The estimated values of direct as well as indirect band gap energy were found to be 3.2 eV and 2.7 eV respectively.

X. Yan and his co-workers [124] reported the preparation of CuS, SnS and ZnS nanopraticles via conventional and microwave hydrothermal techniques. Zinc nitrate, copper nitrate, tin chloride, PVP and thioacetamide were used as starting materials. The reaction was maintained in a stainless steel autoclave at a temperature of 100 ^{0}C, 150 ^{0}C and 200 ^{0}C for 4 hours. The structural properties of the grown samples were analysed by X-ray diffraction and scanning electron microscopy. They reported that the good crystalline materials were obtained in the microwave hydrothermal techniques rather than the conventional

hydrothermal techniques. The optical band gaps of the CuS, SnS and ZnS NPs were determined form the optical absorption study and were found 1.8 eV, 1.3 eV and 3.6 eV, respectively.

SnS nanocrystals with various branched morphologies (nanoflake, nanosheets, nanorods) were prepared via solvothermal technique by S.K. Panda and his groups [125]. Ethylenediamine (EDA), water and their mixture were used as solvent. The as prepared SnS nanostructured were investigated through X-ray diffraction (XRD), scanning electron microscopy (FESEM), transmission scanning electron microscopy (TEM) and reflectance spectroscopy. X-ray diffraction pattern of as synthesized SnS nanostructured confirms the existence of the orthorhombic crystal structured. SEM and EDX analyses presented the shape of surface structure and the presence of purity of the samples. The existence of good crystalline nanostructured was confirmed by TEM analysis. Optical measurements were carried out through reflectance spectroscopy. They reported that the optical band gap of the samples was closed to 1.3 eV.

D. Nithyaprakash et al. [126] reported that SnS nanoparticles were prepared via precipitation method. XRD pattern revealed that the as prepared SnS nanoparticles were orthorhombic crystal phase. No others impurity peaks were observed in the diffraction spectrum. The crystals size was determined from the XRD measurement using Scherrer's formula and was found to be 15 nm. SEM study demonstrated that SnS nanoparticles are in aggregation state. The EDS spectrum presented that the mole ratio of Sn/S in SnS nanocrystals was 1:1. The optical properties of the prepared SnS nanoparticles were studied through UV-VIS spectroscopy and the direct band gap was 1.48 eV. The prepared sample was also investigated through NLO properties.

G. S. Paul et al. [127] demonstrated various type morphologies such as nanoflowers, nanoflakes were synthesized using $SnCl_2.2H_2O$ and NH_2CSNH_2 without any surfactant via

solvothermal route at 200 ^{0}C in different reaction times (1 hour, 3 hours and 5 hours). Ethylenediamine (EDA) was used as solvent. They reported from XRD studies that pure SnS crystal phase was present. Surface micrograph and the chemical compositions of the powder SnS nanostructured were investigated through SEM and EDAX analysis. TEM analysis suggested that the grain sizes were enhanced with the rise of growth time. Thermal stability of the prepared SnS samples have been studies via thermogravimetric analysis (TGA) with the variation of temperature ranging from 30 ^{0}C to 900 ^{0}C. Two kinetic models have been employed to determined Ar. Kinetic parameters. The variations of dark conductivity with the temperature of the SnS nanostructured thin films were studied and the activation energies were also determined using Arrhenius equation.

Q. Han and his groups [128] synthesized different morphologies of SnS architectures (nanosheets, nanoribbons and nanorods) with the variation of some experimental conditions (reaction temperature, reaction time and the molar ratios of reactants) via solvothermal route. Tin dichloride (SnCl$_2$·2H$_2$O), ethylxanthate (C$_2$H$_5$OCS$_2$K) were used as reactants and DMF solution was used as solvent. The reaction was carried out at 180 $^{\circ}$C for 24 hours. The as-prepared samples were studied structurally through XRD, SEM, TEM, and optically through UV–vis absorption spectroscopy, PL spectra. They reported that with the change of molar ratio of the chemical reagents, one type of superstructure have been changed to another superstructure. Besides, capping agents take place a major role for the formation of various shaped SnS nanostructure. UV-vis absorption spectra of the SnS nanostructures have been studied in the optical range (200 nm to 800 nm) and calculated their optical bang gap energy. Room temperature PL spectra of the SnS nanostructures were also recorded and a broad emission peak situated at about 409 nm was observed.

L. Ren et al. [129] synthesized uniform spherical like SnS nanocrystals via solution based chemical route followed by the reaction temperature were selected at 120 °C, 140 °C

and 180 °C. Tin dichloride was used as the source of tin, thioacetamide was used as the

source of sulphur and hydrazine hydrate - based diethylene glycol was used as the reaction

medium. The as-prepared SnS NPs were studied and characterized by X-ray diffraction

(XRD), transmission electron microscopy (TEM) and high resolution transmission electron

microscopy (HRTEM), energy dispersive spectrometry (EDS), and UV-vis-NIR

spectroscopy. The as grown SnS NPs exhibits orthorhombic crystal structure. The particle

diameter has been calculated from the XRD study and was found 8.0 nm, 10.1 nm and 13.2

nm corresponding to the reaction temperature of 120 °C, 140 °C and 180 °C respectively.

TEM and HRTEM result suggested that spherical like SnS NPs were obtained and they also

reported that with increase of reaction temperature the crystal size increases. The EDS spectra

revealed that the prepared SnS NPs maintained good stoichiometric ratio of Sn/S. Optical

properties of the prepared SnS NCs have been studied through UV-vis-NIR spectroscopy and

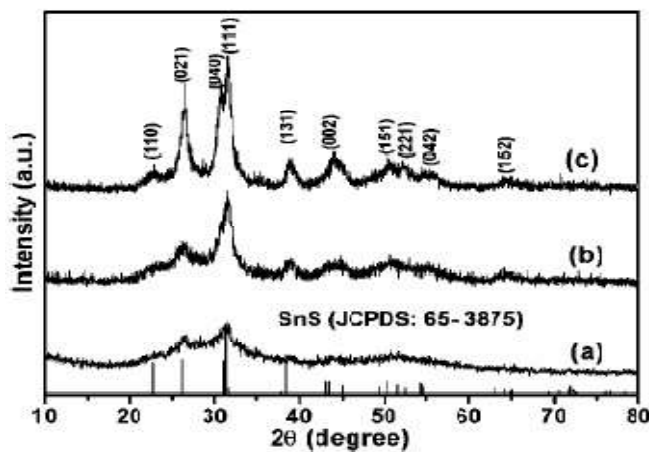the calculated indirect band gap was ~1.1 eV.

Fig. 1.13. XRD patterns of the SnS NCs synthesized at reaction temperatures of (a) 120 °C, (b) 140 °C and (c) 180 °C. [129]
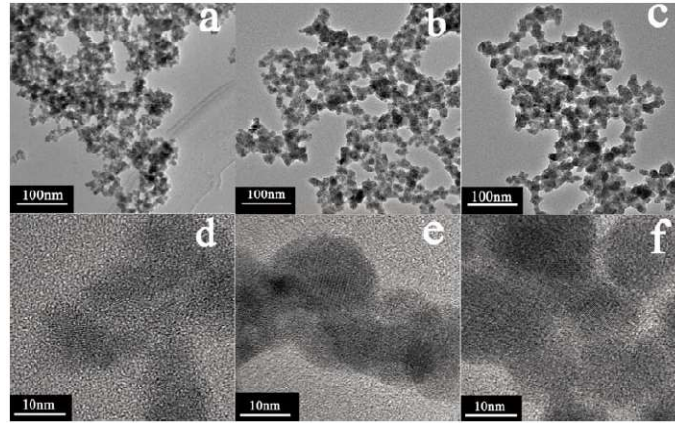
Fig. 1.14. TEM and HRTEM images of SnS NPs prepared at 120 °C (a, d), 140 °C (b, e), 180 °C (c, f).[129]

Y. A-Kalandaragh and his group [130] reported that SnS nanoparticles were prepared by ultrasound irradiation method at room temperature using tin chloride and sodium sulfide. Structural morphological and optical properties of the prepared SnS NPs have been analyzed. From structural characterization, they confirmed that the prepared sample belongs to the orthorhombic crystal phase with the grain size of 3.2 nm. The particle diameter was also calculated from Debye–Scherrer formula and was found to be 4 nm. The UV-vis absorption study measures the band gap energy of the sample which was 1.74 eV. Comparative studies have been analysed between experimental and theoretical results. They reported that theoretical results are good agreement with the experimental results due to the quantum confinement effect of SnS NCs.
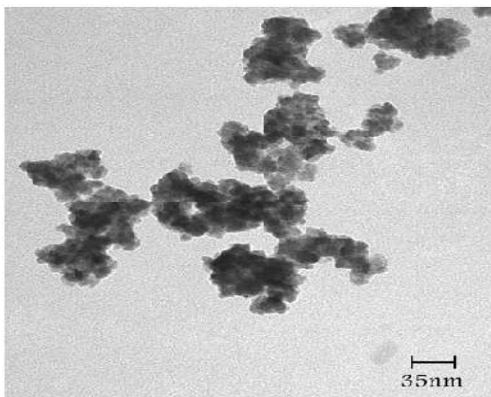

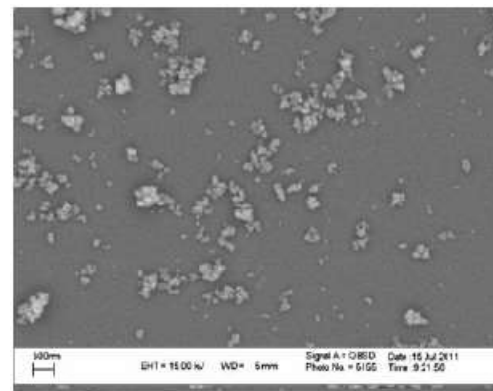**Fig.1.15**. TEM image of the as-prepared SnS NCs [130]
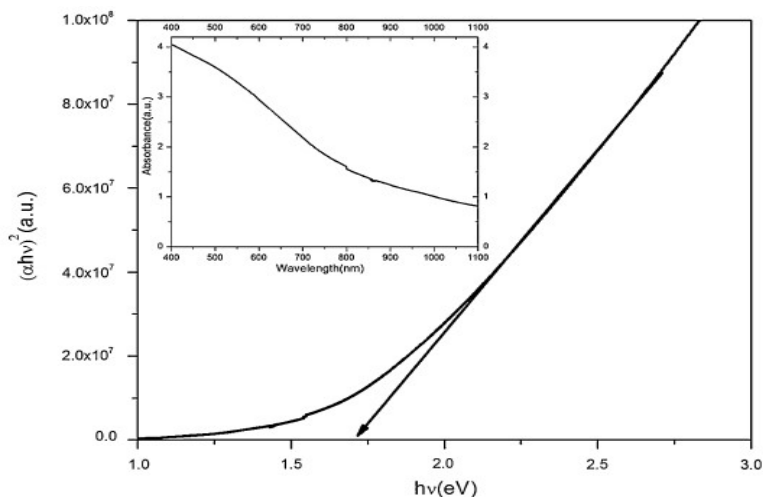
Fig. 1.16. SEM image of the as-prepared SnS NCs [130]

Fig. 1.17. Plot of $(\alpha h\upsilon)^2$ vs. $h\upsilon$ and UV-vis absorption curve of the as-prepared SnS NCs.[130]

C. Chinnasamy et al. [131] synthesized zinc oxide Nano particles (ZnO) by green method. CostusIgneus leaf extract were used as both reducing as well as capping agent. The prepared ZnO nanoparticles were characterized by XRD, UV-vis absorption spectroscopy, FTIR, SEM and EDAX analysis. The SEM and XRD analysis confirmed that the particles are in spherical shape with 31nm particle size. The as synthesized ZnO nanopartcles showed an absorbance peak located at 212nm.The EDAX spectrum confirmed the formation of ZnO NPs.

S. R. Bera et al. [132] prepared CdTe NPs by simple, eco-friendly and cost effective green approach at room temperature. Thevetia peruviana leaf extract was employed as a capping agent. The as prepared sample was analysed structurally by XRD, TEM, AFM, and optically by UV-vis absorption spectroscopy, PL spectroscopy and FTIR spectroscopy. The X- ray diffraction pattern confirmed that the as prepared CdTe NPs are the mixture of cubic and hexagonal crystal phase. TEM analysis found that the crystal size was in the range of 4 – 6 nm. From optical absorption study, they determined the band gap energy of the sample. The as prepared CdTe NPs shows an emission peak situated at 504 nm.

P. Kouvaris and his co-workers [133] reported the synthesis and characterization of metal nanoparticles (Ag) by an eco-friendly and simple route through green method. Arbutus

Unedo leaf extract has been used as reductant as well as stabilizer simultaneously. The as prepared silver nanoparticles were studied by TEM and HRTEM, UV-vis spectroscopy. From UV-vis spectroscopy study, they reported a sharp peak of Ag nanoparticles were detected at 436 nm. HRTEM image confirmed the crystalline behaviour of Ag nanoparticles. From TEM study, they determined particle size of Ag NPs was in the range between 3 and 20 nm.

N. Mayedwa and his groups [134] reported the biosynthesis of $ZnSnO_3$ NPs using Aspalathus Linearis extracts used as reducing as well as capping agents. The as prepared NPs were investigated by X-ray diffraction (XRD), HRTEM, HRSEM, Raman spectroscopy, UV-Vis absorption spectroscopy and FTIR spectroscopy. The XRD image of the green synthesized NPs is a good agreement with orthorhombic perovskite crystal structure of $ZnSnO_3$. No other impurity diffraction peaks were observed. The crystal size of $ZnSnO_3$ nanoparticles was found out with the help of Debye–Scherrer formula was 18.5 nm. The internal and surface morphology were investigated through HRTEM and HRSEM analysis and confirmed the polycrystalline nature of the nanocomposite. UV-vis absorption study demonstrates an absorption peak at 354 nm with optical band gap energy 3.50 eV.

D. Ayodhya et al. [135] reported the preparation of CdS nanoparticles by the green method via Calotropis gigantea leaf extract, used as a capping agent. The as synthesized capped CdS nanoparticles were investigated thoroughly by different tools and techniques. The XRD pattern exhibited the cubic zinc blende structure of CdS. The average crystal diameter of uncapped and Calotropis gigantea capped CdS nanoparticles was found 18 nm and 12 nm respectively. Spherical shaped particles (particle size 20 nm) were studied in TEM image. They reported that, an increase in the optical band gap energy in CdS nanoparticles compared to bulk CdS as confirmed by UV-vis absorption study. Zeta potential and DLS study revealed that as prepared CdS nanoparticles were steady in aqueous solution.

W. Cai et al. [136] synthesized SnS microflowers by solvothermal process with the assistance of biomolecule. They have used L-cysteine as the sulfur source as well as complexing agent. The structural, morphological and optical properties of the as synthesized sample were analysed and studied by various techniques. XRD study determined the crystal structure of the nanoparticles. From TEM analysis they reported that a rod shaped nanoplate of width 500 nm and length of few micrometers were observed. FESEM image exhibits that the SnS sample consists of large number of microflowers and the size of the microflowers were the range in between 10–25 micro-metres. The UV–vis absorption spectra demonstrated that the SnS microflowers have a strong absorption in the visible region.

1.2.2. Gas Sensor

A. muthuvinayagam et al. [137] developed SnS pellet using SnS nanopowder combined with PVA as a binder. The prepared SnS pellet was annealed at 300 ^{0}C for 1 hour. The width of the pellet was approximately 5 mm. They used silver paste used as ohmic contact. The sensor was kept in static gas chamber under the flow of LPG gas and studied its electrical parameters using keithley electrometer (model no 2400). They have studied gas sensing sensitivity of SnS NPs in different temperatures ranging from 200 ^{0}C to 400 ^{0}C under fixed LPG concentrations (500, 1000,1500 and 2000 ppm). They found that the gas sensing sensitivity increases with the increase of working temperature and reached a highest sensitivity value at 340 ^{0}C, then decrease in the sensitivity value with further raise of the working temperature. They have also studied the variation of sensitivity with LPG concentration under fixed temperatures, variation of sensitivity with exposure time (min) under constant temperatures, variation of resistance with exposure time (min) under fixed temperature (300 ^{0}C) as well as gas concentration (1000 ppm) of SnS NPs. They reported that the response time was around 50-60 s and recovery time was varied from 80-90 s.

H. Karami et al. [138] fabricated a gas sensing device (microchip) by copper electroless process. The surface of the gas sensing device was covered by SnS-SnO_2 nanocomposite homogenous solution ultrasonicated via acetone. The fabricated microchip was dried at 100 °C for 10 min. Different target gases such as H_2O, NH_3, O_2, CO, H_2, and Town gas were flowed to the surface of the microchip of SnS-SnO_2 nanocomposite and studied its gas sensing properties. They reported that among these gases O_2 shows good response. Therefore, they have used the microchip of SnS-SnO_2 nanocomposite as O_2 gas sensor. They have studied the relationship between response sensitivity with O_2 concentrations in different operational temperature (25, 75 and 128 ^{0}C). They reported that the adsorption and desorption time of the O_2 gas on the nanocomposite were found to be 52 s and 38 s respectively.

A. Gaiardo and his groups [139] fabricated chemoresistive gas-sensors using Cadmium Sulfide and Tin (IV) Sulfide nanoparticles. They have investigated the fabricated sensors in two different modes (thermo and photo activation mode). Besides, they also studied the electrical behaviour i.e selectivity, sensitivity and stability of the sensors. The achievement of the gas sensing response of the sensors was performed at working temperatures ranging between 150 ^{0}C and 300 ^{0}C for Tin (IV) Sulfide based sensors, whereas for CdS based sensors it was in the range of 150 ^{0}C and 350 ^{0}C. They observed that the best sensitivity of the sensors was found at an operating temperature 300 °C. From the selectivity calibration curve they reported that CdS nanoparticles based sensor were selective to -OH groups, whereas SnS_2 based sensor were selective to aldehydes, ketones and -OH group of the alcohols. They have also studied the gas sensing sensitivity (relationship between the responses and gas concentration) as well as sensor stability (responses vs. time in min) over four weeks of the sensors. The response time and recovery time was also determined and were found to be approximately few minutes for both sensors.

J. Wang and his co-workers [140] fabricated NO_2 gas sensor from thin single crystal of SnS. They deposited SnS thin crystals on n-Si substrate enveloped with a SiO_2 thick layer. The Cr alloy layers have been used as electrodes. Various test gases such as SO_2, CO, NH_3, HCHO and NO_2 have been flowed to the sensor, among them NO_2 shows best response in sensitivity. They reported that, the sensing response for SO_2, CO, NH_3, HCHO (1 ppm) was ~1%, whereas for NO_2 it was ~60%. They also studied the change in voltage of the sensor with real-time under the increase of NO_2 gas concentrations (0.1 to 1 ppm) at 298 K. They reported that the resistance of sensor decreases due to the oxidizing character of NO_2. The change of resistance in percentage versus NO_2 concentration has been also studied. The selectivity coefficient (Q values) of the target gases has been estimated.
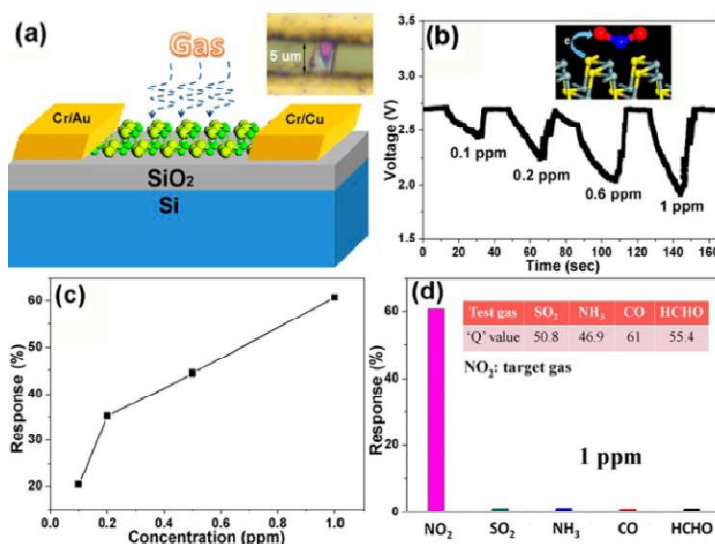

Fig. 1.18. (a) Schematic diagram of SnS gas sensor device. Optical image of device (inset). (b) Real-time voltage relationship under exposure of NO2 gas with increased concentration. The electron transfer mechanism (inset) from SnS to NO2. (c) Plot of response curve as a function of gas concentration. (d) Selectivity of the sensor of the test gases (1 ppm). The Q values of the test gases.[140]

F.-F Hu et al. [141] studied the sensing performance of SnS monolayer for different gas molecules such as NH_3, H_2O, NO_2 and CO with the help of first-principles calculation. The excellent performance of gas sensor based on SnS monolayer was attained. They have studied and calculated some parameters related to the sensing properties. They reported that

NO$_2$ adsorption on the monolayer of SnS possess biggest adsorption energy value of -0.9 eV, modest charge transfer value of -0.307 e. The selectivity and sensitivity to NO$_2$ gas molecules of SnS monolayer based sensor was studied. They experimentally observed that with the adsorption of NO$_2$ gas molecule on the monolayer of SnS changes the current and therefore changes the dynamic resistance.

Rui Li et al. [142] constructed NH$_3$ gas sensor based on SnO$_2$/SnS$_2$ nanotube on polyethylene terephthalate (PET) substrate using photolithographic technique. They investigated the sensing behaviour of both SnO$_2$/SnS$_2$ and pure SnO$_2$ nanotubes sensors under the exposure of NH$_3$ gas in different concentrations (10–500 ppm) at room temperature. They reported that SnO$_2$/SnS$_2$ nanotubes sensor revealed highest sensitivity of 2.48 (100 ppm NH$_3$), whereas it was 1.25 (100 ppm NH$_3$) for SnO$_2$ nanotubes sensor. From the real-time versus dynamic response characteristics curve of the SnO$_2$/SnS$_2$ nanotube sensor they determined the response and recovery time were found to be 21 s and 110 s respectively. The selectivity of the SnO$_2$/SnS$_2$ nanotube sensors was also studied by exposing different gases at (500 ppm) such as acetone, ethanol, ammonia (NH$_3$), toluene, and chloroform. They reported that SnO$_2$/SnS$_2$ nanotubes sensor demonstrated higher sensing response to NH$_3$ than the other gases. Mechanical stability of the SnO$_2$/SnS$_2$ nanotubes sensor was also studied.

Y.-H. Kim et al. [143] prepared two dimensional SnS$_2$-based NO$_2$ gas sensors with integrated microheater by micro-electromechanical systems (MEMS). They have studied the NO$_2$ sensing activity of SnS$_2$-based NO$_2$ sensors with the increase of operational temperature. They reported that the optimal sensitivity of the sensor (with 10 ppm NO$_2$) was attained at an operating temperature of 250 °C rather than 25 °C and 150 °C. The sensor displayed a highest sensing response of 1190.1% with response/recovery times of 6/40 s at 250 °C. Sensing response of the fabricated NO$_2$ gas sensor in different NO$_2$ concentrations (0.5 and 100 ppm) at a fixed operating temperature of 250 °C was studied. The optimal sensing response of

2264.8% and response time of 4 s was achieved when the concentration of NO_2 gas was 100 ppm. They also studied the performances of selectivity of the sensor in presence of NO_2 (1 ppm), hydrogen (10000 ppm), ethanol (1000 ppm), CO_2 (30000 ppm), and acetylene (2500 ppm) gases and found that the sensing response of NO_2 was extensively higher than the other gases.

Y. Li et al. [144] fabricated two-Dimensional SnS_2-based oxygen gas sensor and studied its gas sensing properties in the dark as well as under UV radiation. The real-time dynamic response of the oxygen gas sensor in different oxygen gas concentrations (0 to 20 % vol.) were studied in dark at a working temperature of 150 °C. The dynamic response of the oxygen gas sensor in different temperature and UV illumination were also recorded. They reported that the sensing response decrease with the decreasing of working temperature under dark situation, whereas there was a little fall of the sensing response with the reduction of working temperature under UV illumination. The selectivity of the sensor towards the various gases and vapours at 150 °C as well as in dark condition was also examined. They reported that the highest response in sensitivity was detected for NO_2 gas.

D. Gu and his groups [145] fabricated SnO_2/SnS_2 heterojunction based gas sensor with Au as an electrodes. The SnO_2/SnS_2 heterojunction based sensor displayed good sensitivity and selectivity to the various concentrations of NO_2 gas ranging from 1 ppm to 8 ppm at 80 °C. They reported that the higher sensing response of the fabricated SnO_2/SnS_2 heterojunction based sensor towards NO_2 gas compared to the SnS_2 based one could be recognized due to additional transfer of charge between SnO_2/SnS_2 interfaces. They also investigated the dynamic response graph of the fabricated sensors at an oxidizing temperature of 300 °C under different time. They have also done a comparative study of the three sensors on the basis of sensing response towards NO_2 gas (8 ppm) at 80 °C. They found that the SnO_2/SnS_2 based sensor revealed the highest sensing response. The response and recovery

time of the SnO$_2$/SnS$_2$ based sensor to NO$_2$ gas (8 ppm) was estimated and found to be 159 s

and 297 s respectively.

W. Shan et al. [146] fabricated ethanol gas sensors based on SnS nanosheets and

investigated its sensing properties. The gas sensing properties of the fabricated sensor was

studied under 100 ppm ethanol gas concentrations at working temperatures varied from room

temperature to 160 $^{\circ}$C. The dynamic response curves of the SnS nanosheets based sensors

was also investigated in different ethanol gas concentrations (1 ppm to 100 ppm) at 160 $^{\circ}$C.

They found that the sensors displayed an excellent sensing response of 14.86 (100 ppm) at an

operating temperature of 160 $^{\circ}$C. The rapid response and recovery times were estimated and

found to be 23 s and 26 s respectively. The selectivity of the sensors towards various test

gases such as ethanol, acetone, methanol, toluene, benzene, formaldehyde, acetaldehyde and

water vapour (100 ppm) was studied at a working temperature of 160 $^{\circ}$C. The sensors

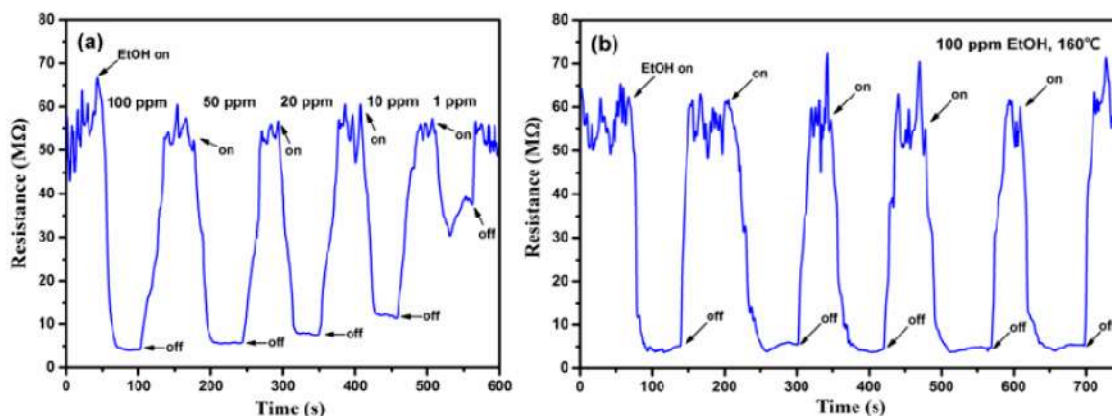exhibited an excellent selectivity for the recognition of ethanol gas over the other gases.

Fig. 1.19. (a) Dynamic gas sensing performance of SnS nanosheets under ethanol in different concentrations (1 ppm to 100 ppm) at 160 ^{0}C (b) Five reversible cycles of SnS nanosheets under 100 ppm ethanol at 160 ^{0}C. [146]

Q. Sun and his co-workers [147] developed SnS$_2$/SnS p-n heterostructures based NO$_2$

gas sensor through drop-dry method. The gas sensing performance (selectivity, sensitivity

and stability) of the fabricated sensors was studied thoroughly. The dynamic response curve

of the SnS$_2$/SnS heterostructures based sensor toward NO$_2$ gas in different concentrations

(0.125 to 8 ppm) was studied at room temperature. They reported that there is an increasing trend of the sensing response with the rise of NO_2 gas concentrations. The sensing response of SnS_2/SnS heterojunction based gas sensor showed an optimum sensitivity of 660% toward 4 ppm NO_2 gas concentrations at room temperature. The higher sensitivity of the sensors was due to the increased of electron transfer between SnS_2/SnS interfaces. They also reported that the as fabricated sensor was more selective to NO_2 gas than the other test gases. The mechanical stability of the SnS_2/SnS heterojunction based sensor was also studied for four months.

M. F. Afsar et al. [148] fabricated acetone and alcohols sensor based on SnS nanoflakes. The dynamic response of the fabricated sensor was investigated under 10 ppm of acetone, ethanol, methanol and 1-butanol gas concentrations at the functional temperatures were ranging from 25 ^{0}C to 200 ^{0}C. They reported that the fabricated sensor exhibits the highest sensing response of 1000% at 100 ^{0}C for acetone. The rapid response and recovery times of these fabricated sensors were also investigated for all gases. They also found that the fabricated sensor based on SnS nanoflakes was highly selective to acetone gas at 100 ^{0}C. The long-term mechanical stability of the sensor was also investigated over six weeks with 10 ppm of acetone concentration.
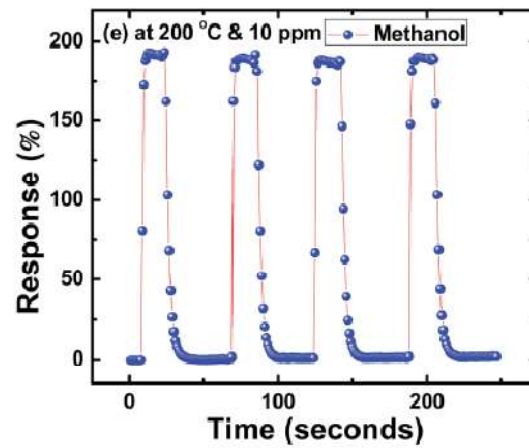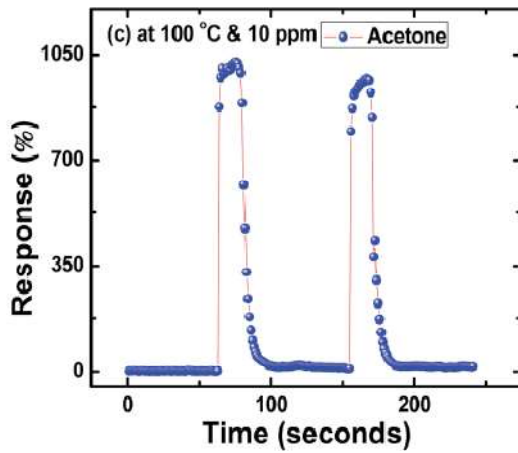
Fig. 1.20. Best response curve of SnS in acetone [148]   **Fig. 1.21.** Best response curve of SnS in methanol [148]
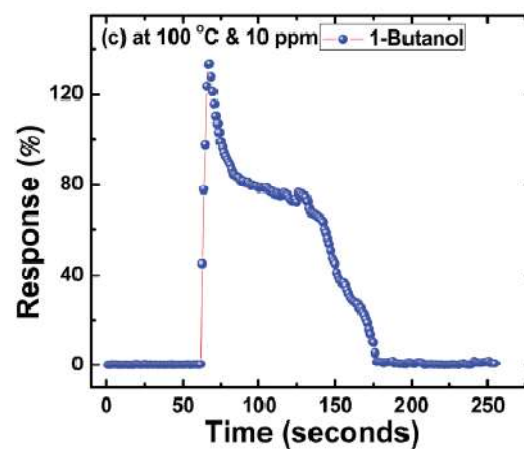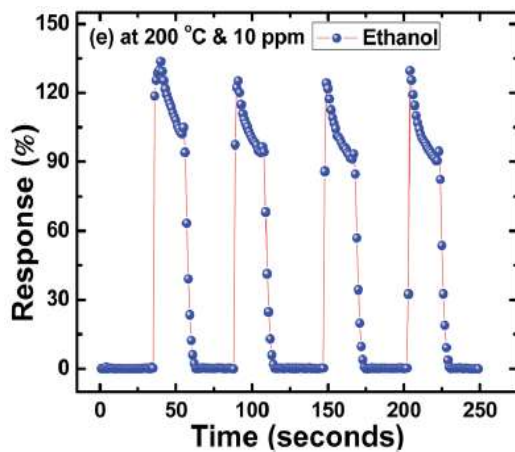

Fig. 1.22. Best response curve of SnS in ethanol [148]   **Fig.1.23.** Best response curve of SnS in 1-butanol [148]

1.2.3. Heterojunction Solar Cell

The fabrication of p-SnS/n-CdS heterojunction thin film solar cells and the performances of the fabricated photovoltaic device were studied by K.T. R. Reddy and his co-workers [149].They have investigated J–V characteristics of the fabricated heterojunction solar cells under the illumination of 100 mW/cm^2. The J–V study exhibits the solar conversion efficiencies of 1.3% was achieved. They also reported that with increase of the thickness of SnS layer increased short circuit current density (J_{sc}) and therefore increased the

fill factor of the solar cells. The open circuit voltage, short circuit current density and fill factor of the SnS/CdS heterojunction solar cells were also determined. They also calculated the series resistance of the solar cells and it was found to be 23 ohm.
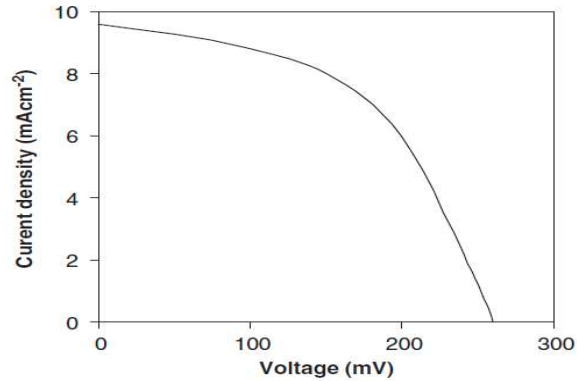

Fig. 1.24. I-V study of SnS/CdS heterojunction solar cell under illumination [149]

H. Li et al. [150] fabricated SnS/CdS heterojunction solar cells in the structure of glass/ ITO/CdS/SnS/In/Ag. The deposition of indium and silver on the SnS layers were used as the back contact. They were investigated the current (I) vs. voltage (V) relationship of the fabricated devices with the variations of CdS buffer layer thicknesses (0 to 80 nm) as well as annealing temperatures (300 ^{0}C to 450 ^{0}C) of the CdS thin films. The performances of the photovoltaic devices were evaluated under dark and light conditions of 4.6 mW/cm^2. They revealed that the short circuit current (J_{sc}) and open circuit voltage (V_{oc}) are mainly depends on the film thickness. Experimentally they observed that optimum performance of the solar cells were achieved for the thickness of the buffer layer of 50 nm and the annealing temperature of 350 ^{0}C. The as fabricated best photovoltaic device showed a power conversion efficiency of 0.0025% under an air mass (AM) 1.5. The lower efficiency of the fabricated heterojunction solar cells was due to the too much higher series resistance.
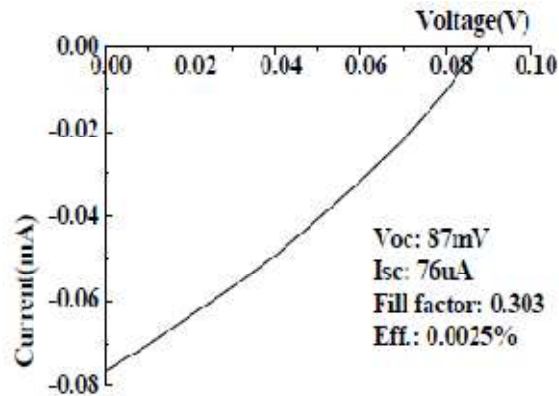
Fig. 1.25. I-V characteristics of SnS/CdS heterojunction under AM 1.5. [150]

B. Ghosh et al. [151] developed SnS/ZnO heterojunction PV devices through vacuum evaporation technique. ZnO layer was employed as window material, deposited on the ITO-coated glass substrate via electrodeposition process. SnS layer was finally deposited on ZnO layer by the vacuum evaporation technique and formed SnS/ZnO heterojunction. Indium metal was utilized as front electrical contact. They studied I–V characteristics of the fabricated heterojunction solar cells under dark and irradiation with air mass 1.5 (1000 W m^{-2}) at 25 °C. The spectral response of the fabricated SnS/ZnO heterojunction was analyzed through spectrophotometer in the range of 400–700 nm. Some electrical cell parameters such as short circuit current (J_{sc}), open circuit voltage (V_{oc}), reverse saturation current (I_0), ideality factor (n), efficiency (η), fill factor (FF) etc. of the fabricated devices were determined. The reported open circuit voltage (V_{oc}) of 0.12 V, short circuit current (I_{SC}) of 39.91 μA and an overall power conversion efficiency of 0.003% were achieved. The poorer conversion efficiency of the PV devices was due to the lattice mismatch between ZnO and SnS layer which diminished the lifetime of the minority carriers.

Table: 1.3

Cell parameters of the fabricated SnS/ZnO heterojunction [151]

Cell parameters	Reported Values
I_m (μA)	26.26
V_m (V)	0.06
I_{SC} (μA)	39.91
V_{oc} (V)	0.120
R_s (kΩ)	5.57
R_{sh} (kΩ)	1.64
FF	0.33
n	1.28
η (%)	0.003
I_0 (μA)	1.005
Cell area	0.4 cm^2

H.-S. Yun and his co-workers [152] reported the fabrication of highly efficient TiO_2/SnS heterojunction solar cells using $SnCl_2$ and thiourea complex solution. Au (gold) has been used as electrodes. The fabricated device structured was Au/SnS/TiO_2. The current (J)–voltage (V) characteristics of the TiO_2/ SnS heterojunction was recorded under dark as well as under solar irradiation of 100 mW cm^{-2} with air mass of 1.5G . They reported that the solar cells displayed best power conversion efficiency of 3.8% when the sample maintained the ratio of thiourea /$SnCl_2$ (mol mol^{-1}) was 1:0.7. Besides, with additional $SnCl_2$ post-treatment (SPT), the power conversion efficiency increased to 4.8%.The increased in efficiency of the fabricated solar cells after $SnCl_2$ post-treatment (SPT) was due to decrease in defects associated with the entering of Cl$^-$ ions into the crystal.
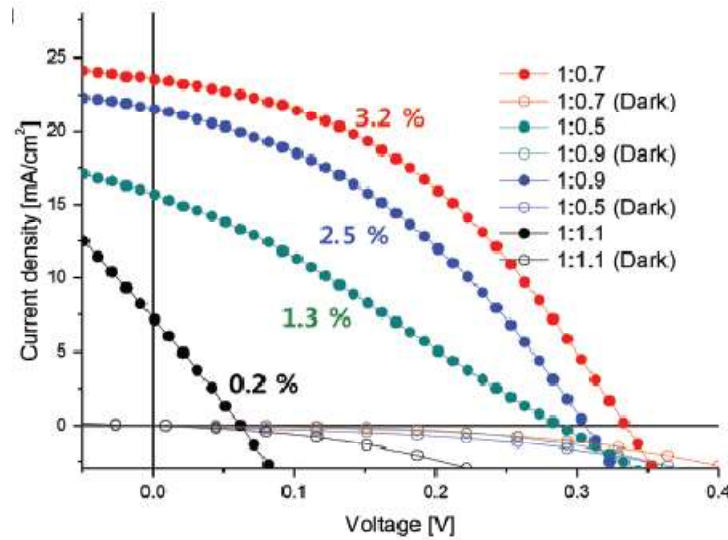
Fig. 1.26. J-V curve of the heterojunction in different ratios of thiourea /$SnCl_2$ (1:0.5, 1:0.7, 1:0.9, and 1:1.1). [152]

Z. Wang et al. [153] fabricated bulk heterojunction (BHJ) solar cells with the based on SnS nanoparticles with crystal size 5-10 nm. The structure of the fabricated device was ITO/PEDOT: PSS/SnS:polymer(active layer)/Al. The blending of SnS nanoparticles with the polymer (P3HT and MDMO-PPV) was act as an active layer of the solar cells. The performances of the devices were evaluated through current density (J)–voltage (V) study under different weight percentage of SnS as well as in different annealing time. They reported that the MDMO-PPV based solar cell exhibited the high performances (67 wt% of SnS, at 110 ◦C for 22 h) than the P3HT based solar cell and the power conversion efficiency of the MDMO-PPV based solar cell was found to be 0.021%.

J. J. M. Vequizo et al. [154] developed tin sulfide (SnS)/tin dioxide (SnO_2) heterojunction solar cell using SnO_2 films annealed at different temperatures by electrodeposition process. The SnO_2 layers were also deposited on ITO substrate in different voltages. The photovoltaic behaviour of the fabricated solar cell was recorded with the help of J-V study under dark and irradiation conditions. The open circuit voltage, short circuit current density and power conversion efficiency of the SnS/SnO_2 heterojunction fabricated with SnO_2 window layer annealed at 250 ^{0}C were determined. The reported power conversion

efficiency was in the order of 10^{-2}-10^{-1}%. The energy band discontinuities at the interface of SnS/SnO$_2$ were also determined through XPS measurements. The evaluated valence band offset of SnS/SnO$_2$ heterojunction was approximately 1.85 eV.

F. Jiang et al. [155] prepared a novel p-SnS/n-Si heterojunction solar cell with the structure Mo-glass/p-SnS/n-Si/ITO. Ni–Al metal doted was employed as a face contact. The current vs. voltage measurements of the fabricated SnS/Si heterojunction solar cell was recorded in dark and light condition (AM 1.5G). From the I-V study of the heterojunction under dark condition they found that the junction behaves just like a rectifying diode and the estimated diode identity factor of the junction was close to 2.34, whereas, under light condition they determined the open circuit voltage (V$_{oc}$) and short circuit current density (J$_{sc}$) were 289 mV and 1.55 mA/cm^2 respectively. They also determined the fill factor as well as solar conversion efficiency of the heterojunction solar cells were found to be about 37% and 0.17% respectively.
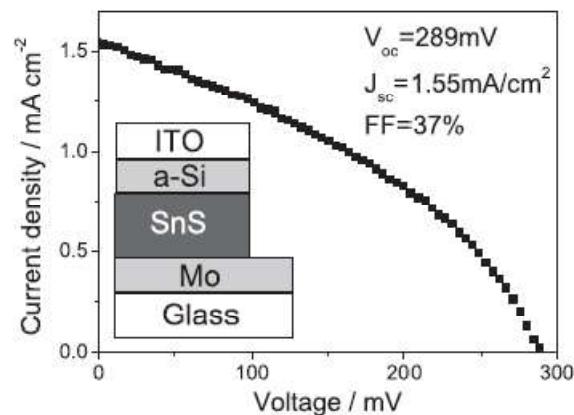

Fig. 1.27. I-V study of the SnS/Si heterojunction solar cell under illumination. [155]

S.A. Bashkirov et al. [156] prepared Mo/p-SnS/n-CdS/ZnO heterojunctions and studied its structural, chemical as well as photo electric properties. The heterostructure consists of a p-SnS layers were deposited on Mo-covered glasses at 270–350 °C, an n-CdS layers were deposited on Mo-coated SnS film and a ZnO bilayer. The structural

characterization of the heterostructure was studied by SEM and AES analysis. The photovoltaic properties of the fabricated heterostructure were investigated by I-V study in dark as well as illumination with the power density of 30 mW/cm^2. From the I-V curve of the heterojunction they determined various cell parameters such as short circuit current, open circuit voltage, maximum power density, fill-factor and light conversion efficiency. They found that the best cell parameters were achieved for the heterojunctions fabricated using SnS films (deposited at 350 °C with 5 μm film thickness).

Table: 1.4
Cell parameters under irradiation of 30 mW/cm^2 [156]

The best cell parameters under illumination of 30 mW/cm^2.

Active area	0.2 cm^2
n	4
R_s	40 Ω
R_{sh}	350 Ω
I_0	0.20 mA (1.00 mA/cm^2)
I_{ph}	0.73 mA (3.68 mA/cm^2)
I_{SC}	0.72 mA (3.63 mA/cm^2)
V_{oc}	132 mV
FF	0.29
P_{max}	0.135 mW/cm^2
η	0.5%

A. Stavrinadis and his groups [157] fabricated SnS/PbS hetrojunction solar cells having structure ITO/SnS/PbS/Al, contained a layer of SnS nanoparticles grown at 80 °C and 120 °C. The photovoltaic performances of the fabricated solar cells were studied through current-voltage characteristics in dark and under illumination with power density 80 mW cm^{-2} (air mass 1.5). They reported that the best performance of the fabricated heterojunction was obtained for 80 °C EAA SnS/PbS 920 nm. The open circuit voltage (Voc), short circuit current (Isc), fill-factor (FF) and efficiency (η) of the heterojunction solar cells constructed in different conditions were estimated from I-V study. Among them the best power conversion efficiency of the SnS/PbS hetrojunction was found to be 0.5%.

P. Jain et al. [158] reported a comparative study in between plasmonic (ITO/ PEDOT: PSS/SnS:Ag/Al) and non-plasmonic (ITO–PEDOT: PSS–SnS–Al) heterojunction solar cells on the basis of their photovoltaic performances. The photovoltaic behaviour of the fabricated

47

heterojunction was studied through J-V measurements with the variation of active layer thickness (350 nm- 800 nm). The current vs. voltage measurements were recorded under illumination with the source intensity of 100 mW/cm^2, 1.5 AM. They reported that there were enhanced of the power conversion efficiency with the increasing of active layer thickness. They also found that the optimum conversion efficiency was achieved for the plasmonic solar cells over the non-plasmonic solar cells with 800 nm active layer thickness. This enhancement of the conversion efficiency of the plasmonic solar cells was due to the scattering effect of Ag nanoparticles within the solar cell.

S. L. Mousavi and his co-workers [159] fabricated polymer solar cells based on pure SnS, Zn-doped SnS and NPs free sample. The device architecture was ITO/PEDOT: PSS/P3HT: PCBM/Al and ITO/ PEDOT: PSS/P3HT: PCBM: NPs/Al. The device performances were made through J-V study of the solar cells. The photovoltaic cell parameters of the fabricated devices such as open-circuit voltage, short-circuit current, fill factor, power conversation efficiency were determined under solar illumination of power density 100 mW/cm^2 with 1.5 AM. They reported that the Zn doped SnS Nps based device improved its efficiency compared to the pure SnS as well as NPs-free sample based devices. The highest J_{sc} (12.65 mA /cm^2), V_{oc} (0.55 V) and PCE (3.75%) were exhibited for the Zn doped SnS Nps based solar cell.
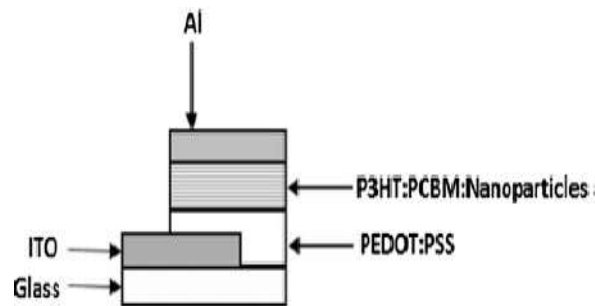

Fig. 1.28. Architecture of the fabricated device [159]

Table: 1.5

Photovoltaic parameters of PSCs [159]

Sample/Photovoltaic parameters	V_{oc} (V)	J_{sc} (mA/cm^2)	FF	PCE (%)	EQE (%)	R_{ss} (Ω/cm^2)	R_{sh} (Ω/cm^2)
P3HT:PCBM	0.55 ± 0.027	9.40 ± 0.47	0.48 ± 0.024	2.49 ± 0.12	36.05 ± 1.79	19 ± 0.9	800 ± 40
P3HT:PCBM + Zn(0)	0.55 ± 0.027	11.84 ± 0.59	0.55 ± 0.027	3.58 ± 0.18	52.52 ± 2.63	14 ± 0.7	1000 ± 50
P3HT:PCBM + Zn(1)	0.54 ± 0.027	10.30 ± 051	0.51 ± 0.025	2.89 ± 0.14	40.75 ± 2.04	16 ± 0.8	769 ± 38
P3HT:PCBM + Zn(2)	0.55 ± 0.027	12.65 ± 0.63	0.54 ± 0.027	3.75 ± 0.19	57.77 ± 2.79	14 ± 0.7	749 ± 37
P3HT:PCBM + Zn(3)	0.55 ± 0.027	11.20 ± 0.56	0.53 ± 0.026	3.27 ± 0.16	44.07 ± 2.28	18 ± 0.9	803 ± 40

1.2.4. Dye Sensitized Solar Cell

X. Chen et al. [160] developed dye-sensitized solar cells (DSSCs) based on SnS nanosheets, SnS nanowires and SnS$_2$ nanosheets counter electrodes (CEs). The photocurrent vs. voltage of the fabricated DSSC with different counter electrodes was investigated. They compared the energy conversion efficiencies among the fabricated DSSC with various CEs. They reported that the power-conversion efficiency of SnS nanosheets CEs based DSSC (6.56%) was comparable to platinum CEs based DSSC (7.56%), while the efficiencies of SnS nanowires and SnS$_2$ nanosheets CEs based DSSCs were 5.00% and 5.14% respectively. The series resistance (R$_s$), charge-transfer resistance (R$_{ct}$), double layer capacitance (C$_{dl}$), warburg impedance (Z$_w$) of the fabricated devices were also estimated.

Table: 1.6

Photovoltaic parameters of fabricated DSSCs [160]

Samples	J_{sc} (mA cm^{-2})	V_{oc} (mV)	FF (%)	E_{ff} (%)	R_s (Ω)	R_{ct} (Ω)	E_{pp} (mV)	C_{dl} (μF)	Z_w (Ω)
SnS NSs	17.70	740	50	6.56	6.34	0.94	255	93.6	87.06
SnS$_2$ NSs	13.69	700	54	5.14	6.43	1.22	180	121.0	44.47
SnS NWs	13.50	720	51	5.00	7.26	6.04	396	83.3	16.85
Pt	17.50	720	60	7.57	10.67	3.28	260	3.3	4.51

X. Wang and his groups [161] fabricated dye-sensitized solar cells (DSSCs) with SnS Nanosheets (SnS-S) and SnS Pentahedron (SnS-P), utilized as counter electrode. The current density (J) vs. voltage (V) relationship of prepared DSSCs with different counter electrodes (CEs) were measured under illumination (AM1.5). The photovoltaic parameters such as

short-circuit current (J_{sc}), open-circuit voltage (V_{oc}), fill factor (FF) and solar conversion efficiency (η) were evaluated. They reported that the DSSCs based on SnS-S counter electrode exhibited an excellent solar conversion efficiency of 8.96%, which was superior to that of the SnS-P (8.23%) and Pt (7.72%) counter electrode based DSSCs.
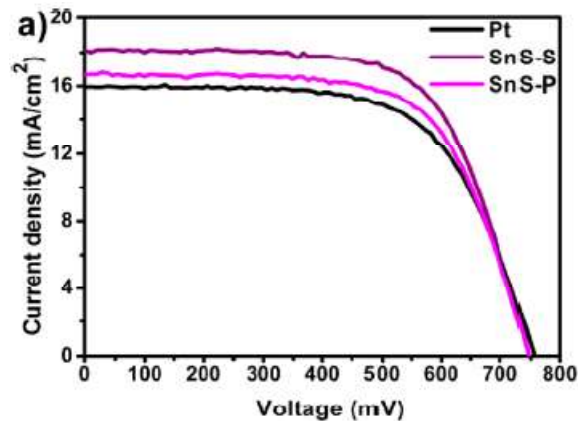

Fig. 1.29. Current vs. voltage characterized of the Fabricated DSSCs under illumination [161]

X. Xin et al. [162] designed a low expenditure, highly efficient N719 dye-sensitized solar cells (DSSCs) using Copper Zinc Tin Sulfide (CZTS) and Copper Zinc Tin Sulfide Selenide (CZTSSe) counter electrodes (CEs). The TiO_2 nanoparticle layer and N719 have been used as photo anode as well as commercial dye respectively. They reported that the best power conversion efficiency (PCE) of 7.37% was achieved for Spin-coated CZTSSe counter electrode based DSSC which was comparable to that of Pt CE (7.04%) based DSSC.
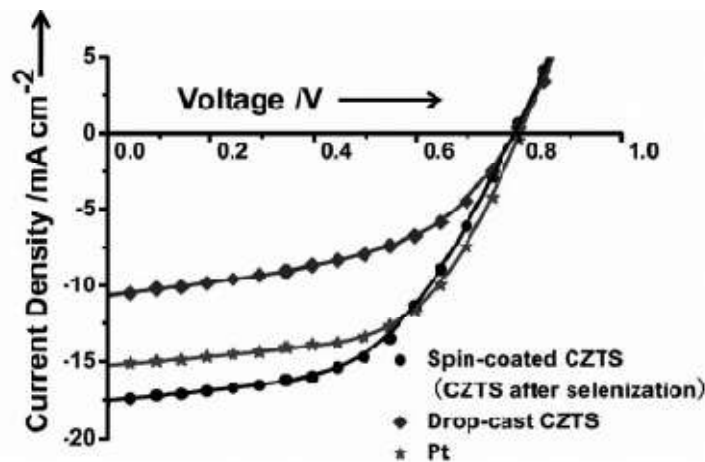

Fig. 1.30. J-V curve of the fabricated dye sensitized solar cells. [162]

N. Ananthi et al. [163] prepared low cost, eco-friendly and efficient dye-sensitized solar cells (DSSCs) with natural dyes Acalypha Godseffia and Epipremnum Aureum leaves extraction as photosensitizes. The current vs voltage characterization of the fabricated dye-sensitized solar cells was studied under illumination conditions. They demonstrated that the performances of Acalypha Godseffia extaction based DSSC (E_{ff}: 4.372%) was superior than the Epipremnum Aureum extaction based DSSC (E_{ff}: 3.362%).

M. A. Azhari et al. [164] reported the fabrication and electrical characterization of the dye sensitized solar cell (DSSCs) based on natural dyes. They have used six types of natural dye such as raspberry, blueberry, turmeric, henna, dragon fruit and senduduk extracted from plants and fruits. These natural dyes have been employed as photosensitizes. Comparative studies on their sensitization have been made. They reported that the Raspberry extraction based DSSC attained the maximum solar conversion efficiency of 0.0568% with short-circuit current (I_{sc}) of 0.0367 mA, open circuit voltage (V_{oc}) of 474 mV and fill factor (FF) of 0.818. The maximum solar conversion efficiency of raspberry plant extraction was due to the presence of high concentration of anthocyanin contain.

A. M. Ammar and his groups [165] prepared dye-sensitized solar cells (DSSCs) using natural dyes. The extractions from spinach leaves, red cabbage and onion were used as sensitizer. The performances of the solar cells were analyzed by the extraction of natural dyes as well as using N-719. The TiO2 layer of 10% concentration was employed as photoanode. The conversion efficiency of 10% TiO2 thin film has been examined and it was found to be 2.239%. Among the natural dye based solar cells, spinach leaves extraction based DSSC showed highest power conversation efficiency of 0.17%. The stability in the conversion efficiencies of the fabricated DSSCs was also observed throughout one week.

Table 1.7

Electrical parameters of the fabricated DSSCs with natural dyes [165]

Dye	J_{sc} (mA·cm^{-2})	J_m (mA·cm^{-2})	V_{oc} (V)	V_m (V)	FF (%)	η (%)
Spinach	0.41	0.309	0.59	0.46	58.75982	0.171253
Onion	0.24	0.158	0.48	0.34	46.63194	0.064723
Red cabbage	0.21	0.156	0.51	0.32	46.61064	0.060145

M. Rossi et al. [166] reported the fabrication and study of low cost dye-sensitized solar cells (DSSCs) based on chlorophylls and xanthophylls plants extract as natural dyes. Chlorophylls were collected from fresh spinach leaves whereas xanthophylls were collected from fruits of red pepper ground. The TiO$_2$ nanoparticles have been used as photoanode. They were characterized the photoelectric behaviour of the DSSCs and were determined the cell parameters such as short-circuit current (J_{sc}), open-circuit voltage (V_{oc}), fill factor (FF) as well as solar conversion efficiency (η). They exhibited a maximum conversion efficiency of 0.72% of the DSSC based on chlorophylls dye was achieved compared to DSSC based on xanthophylls dye.

K. Bera et al. [167] prepared and characterized dye-sensitized solar cell (DSSC) using the extraction three natural dye such as Gerbera jamesonii, Rosa indica and Acalypha wilkesiana. The extractions of natural dyes were used as photosensitizers. They photovoltaic behaviour of the fabricated DSSCs was recorded through current (I)-voltage (V) measurements. Various parameters such as open circuit voltage, short circuit current, power conversion efficiency and fill factor were interpreted from I-V study. They reported that the DSSC based on Acalypha wilkesiana leaves extract dye exhibited highest solar conversion efficiency.
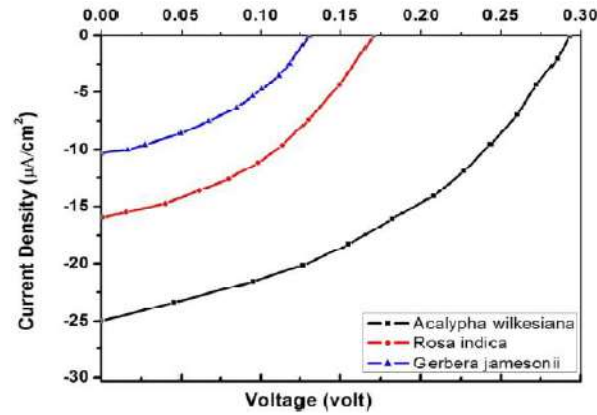
Fig. 1.31. I-V graph of the fabricated DSSCs. [167]

Table: 1.8

Photovoltaic parameters of the DSSCs [167]

Dye solution	Photograph	V_{max} (mV)	J_{max} ($\mu A/cm^{-2}$)	V_{oc} (mV)	J_{sc} ($\mu A/cm^{-2}$)	Fill Factor (FF)	Efficiency η X10^{-2}
Acalypha wilkesiana		92	15.3	293	25	0.40103754	0.29376
Rosa Indica		08	10.2	165	17	0.39272727	0.11016
Gerbera Jamesonii		4	6.4	130	11.7	0.35345168	0.05376

S. R. Bera et al. [168] reported the fabrication of dye sensitized solar cells (DSSCs) based on undoped and Zn-doped CdTe. The extractions of Hibiscus mutabilis flower were used as sensitizer. The characterization of the fabricated solar cells were made using J-V study under dark as well as under light condition. They reported that overall solar conversion efficiency of Zn-doped CdTe based DSSC was higher than the pure CdTe based DSSC.

Table: 1.9

Various Photovoltaic parameters of the prepared DSSCs [168]

Anthocyanin	Samples	V_{max}(Volt)	J_{max}(mA/cm^2)	V_{oc}(Volt)	J_{sc}(mA/cm^2)	FF (%)	Efficiency(η)%
Hibiscus mutabilis	Undoped CdTe	0.5	2.4076	0.609	2.9667	66.63	1.2038
	Zn-doped CdTe	0.57	2.7246	0.692	3.2640	68.76	1.5530

B. Yang and his co-workers [169] fabricated dye-sensitized solar cells (DSSCs) based on SnS_2, RGO and SnS_2- RGO nanocomposite counter electrodes (CEs) using N-719 as commercial dye. The current vs voltage measurements of the fabricated DSSCs were studied. They found that an overall power conversion of the SnS_2- RGO nanocomposite CE based DSSC was found to 7.12% which was larger than the SnS_2 CE and RGO CE based DSSC.

F. Kabir el al. [170] demonstrated the fabrication and characterization of dye-sensitized solar cells (DSSCs) based on two types of natural dyes. Red spinach (red dye) and Turmeric (yellow dye) extract were exploited as dye sensitizers. The TiO_2 nanoparticles were used as electron conductor. The power conversion efficiencies of the fabricated DSSCs based on red dye, yellow dye and the mixture of red and yellow dye were determined. They reported that the combined dyes (40% red+60% yellow) based DSSCs exhibited an optimum conversion efficiencies of 1.078%.

Table: 1.10

Various Photovoltaic parameters of the prepared DSSCs [170]

Combination of Dye	V_{oc}(mV)	I_{sc}(mA)	FF	η%
100% Yellow	499.5	1.575	0.481	0.378
80% Yellow + 20% Red	479.3	2.258	0.457	0.495
60% Yellow + 40% Red	499.3	4.264	0.507	1.079
50% Yellow + 50% Red	458.5	3.728	0.465	0.795
40% Yellow + 60% Red	389.6	2.594	0.431	0.436
20% Yellow + 80% Red	366.1	1.409	0.404	0.208
100% Red	338.4	0.882	0.449	0.134

1.2.5. Interaction of nanoparticles with protein

H. Yang et al. [171] reported the binding of hydrophilic silica NPs and hydrophobic silica NPs with bovine hemoglobin. The as prepared protein−NP complex was studied by dynamic light scattering (DLS) analysis, UV–vis absorption spectroscopy, fluorescence spectroscopy, Raman spectroscopy and FTIR spectroscopy.The particle size of the complex was calculated through DLS study, which proved the interaction of nanoparticles with bovine hemoglobin. The zeta potential and DLS analysis also confirmed that the protein corona has

been formed. The adsorption behaviour of bovine hemoglobin on hydrophilic silica NPs and hydrophobic silica NPs were fitted best by the Freundlich model and confirmed that the adsorption behaviour followed second order kinetics. The UV–vis and FTIR measurements investigated the conformational change of bovine hemoglobin (BHb). From Fluorescence spectroscopy, they studied the conformations as well as the heme degradation of protein.

S. Chakraborti and his groups [172] investigated the binding of polyethyleneimine-functionalized ZnO Nps (ZnO-PEI) with bovine serum albumin (BSA). The binding of BSA to the surfaces of ZnO-PEI were analyzed through isothermal titration caloriemetry (ITC), spectroscopic and computational analysis. The ITC measurements showed that protein−NP complexation was enthalpydriven, signifying the contribution of van der Waals weak interaction occurred in the binding process.
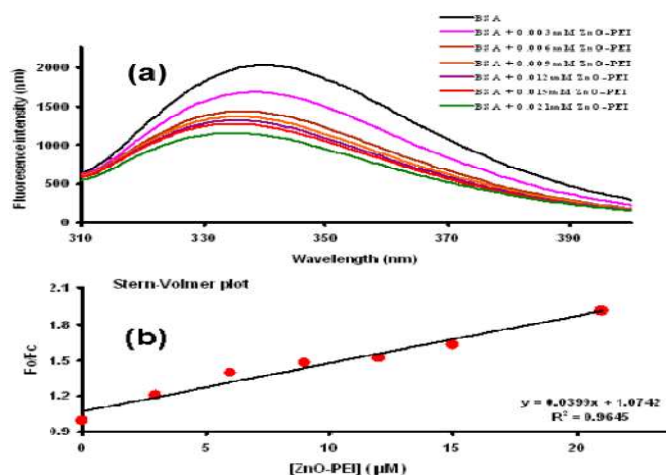

Fig. 1.32. (a) Quenching of BSA fluorescence with the variation of the amount of ZnO-PEI. (b) Stern-Volmer plot of the BSA –NP complex. [172]

The interaction of BSA–NPs was also studied through fluorescence quenching spectroscopy. Fluorescence quenching measurements determined the nature of binding, quenching rate, nature of quenching, type of quenching and binding constant (K_b) of BSA –NP complex. They reported that the quenching was static in nature and the value of K_b was estimated to be 6.4×10^4 M^{-1}. The conformational changes of protein on the surfaces of NPs were also

studied by CD (circular dichroism) spectroscopy. Also, Adaptive Poisson−Boltzmann Software (APBS) was utilized to study the nature of binding, binding location as well as surface electrostatic potential of the BSA –NP complex.

M. A. Jhonsi et al. [173] studied the interaction of uncapped and starch capped CdS NPs with bovine serum albumin (BSA). The interaction of the NPs with the protein was investigated through different tools and techniques. From UV–visible absorption, the apparent association constant and degree of association was evaluated. The binding constant (K_b) of the protein−NP were determined from fluorescence quenching spectroscopy and it was found 6.6 $\times 10^2$ M^{-1}. The higher quenching rate constant of 3.25×10^{11} M^{-1} s^{-1} was determined from time resolved and fluorescence measurements, which confirmed that the quenching was static in nature. The conformation changes of protein (BSA) were also investigated by the UV–vis absorption as well as synchronous fluorescence spectra.

S. Saha et al. [174] reported the interaction of CdS NPs with bovine serum albumin (BSA). The BSA-CdS NPs interaction, complexation formation and conformational changes of protein (BSA) with the CdS nanoparticles were investigated by microscopic as well as spectroscopic measurements. The UV-vis absorption study confirmed the interaction of CdS nanoparticles with protein through tryptophan and tyrosine. The binding constant (K_b) and Hill constant (n) of the BSA –NPs complex was also determined. The conformational changes of protein model on the surfaces of CdS NPs were analysed from fluorescence spectroscopy.

B. Hemmateenejad et al. [175] investigated the bimolecular interaction of human serum albumin (HSA) to the surfaces of ZnS NPs through florescence spectroscopic measurements. The quenching of protein (HSA) upon the association of ZnS NPs in the florescence spectra confirmed the binding of ZnS NPs with HSA. The florescence

spectroscopic measurements exhibited that the nature of quenching mechanism was in static type. Stern–Volmer constant (K_{vs}) and quenching rate constant (K_q) of the binding of HSA to ZnS NPs was estimated from Stern–Volmer plot. The negative values of the thermodynamic parameters confirmed the weak interaction in the binding of ZnS NPs to HSA has been occurred. The location of binding site of ZnS NPs with HSA was also determined. The Synchronous fluorescence spectroscopic measurements as well as the experimental temperature confirmed the conformational changes of HSA molecules due to existences of ZnS NPs.

Table: 1.11

Binding constants and various thermodynamic parameters of ZnS NPs HSA interaction [175]

pH	Temp. (K)	f_a	$K_a\ (\times 10^4\ L\,mol^{-1})$	R^2	$\Delta G\ (KJ\,mol^{-1})$
7.4	310	0.0466	9.67	0.998	−12.86
	304	0.0401	12.4	0.999	−12.87
	298	0.0312	15.8	0.999	−12.88

K. Bera et al. [176] investigated and studied the interaction of ZnS nanoparticles with Lysozyme protein. The ZnS NPs and protein complex were examined through spectroscopic and microscopic measurements. UV-vis absorption spectroscopy confirmed the interaction ZnS NPs with Trp of Lysozyme. They also reported that the ground state complex was formed during the binding process of ZnS NPs and Lysozyme. The quenching of the fluorescence spectroscopy of the protein (tryptophan of Lysozyme) was observed. They calculated the binding constant, the number of binding site in between Lyz and ZnS NPs and it was found to be 2.06 $(mM/L)^{-1}$ and 0.71 respectively, which confirmed the negative cooperative phenomenon. They also observed a fibrillar structure in the TEM image of ZnS NPs and Lyz complex which also confirmed interaction of ZnS NPs with Lyz.

A. K. Bhunia and his co-workers [177] investigated the interaction of bovine serum albumin (BSA) to PbS nanoparticles. The binding of BSA with PbS NPs were studied

through HRTEM, UV-vis absorption spectroscopy and fluorescence spectroscopy measurements. The HRTEM image revealed the formation of soft and hard corona in the interaction of PbS NPs with BSA. They were estimated the shell thickness of BSA which enclosed the hard corona was 8 nm. The fluorescence emission quenching of BSA upon the association of PbS nanoparticles confirmed the interaction of PbS NPs with BSA through dynamic process. The various thermodynamic parameters have been calculated. They also reported the positive cooperative phenomenon occurred in between PbS NPs-BSA complex. They found that binding in between PbS NPs-BSA complex was electrostatic in nature. The conformational change of protein (BSA) was observed which was due to the hydrophobic interaction in between PbS nanoparticles and protein (BSA).

Y.-L. Wu et al. [178] investigated and illustrated the interaction of CdTe NPs with lysozyme (Lyz) protein. The binding between CdTe NPs and lysozyme (Lyz) protein were analysed through spectroscopic measurements. The fluorescence emission quenching of lysozyme (Lyz) with the addition of CdTe NPs were reported, indicating the interaction of CdTe NPs-Lyz complex. The binding constant (K), number of binding sites (n) and the Stern–Volmer fluorescence quenching constant (K_V) were also calculated. The conformation change of Lyz structure was observed which confirmed the binding of Lyz protein on the surfaces of CdTe NPs. They also reported that the fluorescence quenching mechanism was followed a static quenching phenomenon.

L. Shao and his groups [179] reported the interaction of CdTe quantum dot with a model of protein, bovine serum albumin (BSA) through fluorescence correlation spectroscopy (FCS) study. From experimental studies, they confirmed the interaction between CdTe QDs and BSA. The association constant was estimated and it was found to be $1.06 \pm 0.14 \times 10^7$ M^{-1} in 0.01 M phosphate solution. They interpreted that the electrostatic interaction was mainly responsible for the binding of CdTe QDs with BSA.

M. M. Dzagli et al. [180] interpreted the interaction in between CdSe/ZnS quantum dots (QDs) and bovine serum albumin (BSA). The formation of the bioconjugate (CdSe/ZnS QDs@BSA) were analysed by UV–vis absorption and fluorescence spectroscopic measurements. The UV–vis absorption measurements and the fluorescence quenching of BSA by CdSe/ZnS QDs established the interaction of QDs with BSA. The conformational changes of the bovine serum albumin (BSA) protein was also confirmed the binding of CdSe/ZnS QDs with BSA.